Optical System for a Transversally Blockaded Yb-Rydberg Ensemble

Johnny Schäfer

Bachelorarbeit in Physik angefertigt im Institut für Angewandte Physik

vorgelegt der

Mathematisch-Naturwissenschaftlichen Fakultät
der

Rheinischen Friedrich-Wilhelms-Universität
Bonn

Juli 2025

Ich versichere, dass ich diese Arbeit selbstständig verfasst und keine anderen als die angegebenen Quellen und Hilfsmittel benutzt sowie die Zitate kenntlich gemacht habe.

Bonn, 30.07.2025 Datum

Gutachter: Prof. Dr. Sebastian Hofferberth
 Gutachter: Jun. Prof. Dr. Daqing Wang

Acknowledgements

I would like to thank Prof. Dr. Sebastian Hofferberth for providing me with the opportunity of writing my thesis in the NQO-Group on this topic and learning much from it. I would also like to thank Jun. Prof. Dr. Daqing Wang for being my second examiner. Furthermore I want to thank Tangi Legrand and Eduardo Uruñuela Castillero for their daily support, help and patience. I also want to thank the rest of the YQO-Group members and the NQO-Group as a whole for the great and constructive work atmosphere.

Contents

1	Introduction 1						
2	Setu	p of Ry	ydberg Yb experiment	3			
	2.1	Main e	experiment setup	. 3			
		2.1.1	Limitations and goals for testing	. 5			
		2.1.2	Gaussian Beams	. 5			
		2.1.3	Choice of lens and collimator	. 8			
	2.2	Test Se	etup for Probe Beam Waist Optimization				
		2.2.1	Used components	. 11			
		2.2.2	Alignment strategy	. 16			
3	Test	Experi	iment Methods and Results	19			
	3.1	•	ved waist and used strategy	. 19			
		3.1.1	Presentation of Calibration Strategy	. 19			
		3.1.2	Presentation of analysis strategy	. 23			
		3.1.3	Gaussian Fit model				
		3.1.4	Presentation of measurement results	. 25			
	3.2	Effects	s of the glass plates				
	3.3		llection of probe light				
		3.3.1	Triplet Collimator Adjustment				
4	Con	clusion	1	35			
	Outle	ook		. 36			
A	App	endix		37			
	A. 1	Gaussi	ian fits for beam profile measurements	. 37			
	A.2	Beam	profile	. 37			
	A.3	Beam	quality factor M^2	. 37			
	A.4	Triplet	t Collimator Focal Length Calculation	. 37			
Bil	oliogi	aphy		43			
Lis	t of F	igures	:	45			
LIS	it OT I	ables		49			

vi 30th July 2025

Introduction

Precise control of laser beams is essential in atomic physics, to achieve desired manipulation of degrees of freedom of the atoms. Factors such as frequency stabilization, intensity regulation, and the alignment and quality of optical components all play critical roles. Optimizing these parameters is important for optimal outcomes in the experiments. This level of precision is particularly critical in experiments involving Rydberg atoms, which rely on tightly controlled laser excitation to access highly excited electronic states.

Rydberg atoms exhibit strong, long-range dipole-dipole interactions, leading to the so-called Rydberg blockade effect. In this regime, the excitation of one atom to a Rydberg state suppresses the excitation of nearby atoms within a characteristic blockade radius [1]. This effect forms the basis for exploring strongly interacting photonic systems at the single-photon level.

In order to isolate and analyze these interactions, a so called two photon excitation scheme can be used [2]. This scheme uses a probe beam to drive from a ground state to an excited state and a control beam which drives from the excited to the desired Rydberg state.

In order to improve on the simplicity of the design of such Rydberg experiments, the effective dimensionality of the interacting atomic systems can be reduced to only one dimension. This enables clearer conceptual understanding and quantitative comparison with theoretical models [1].

Such a reduction for the experimental dimension can be achieved by tightly, focusing the probe laser to a sufficiently small beam waist. This spatial confinement of the excitation volume, makes sure that only atoms along the narrow axis are excited, thus only allowing one-dimensional interactions.

However, achieving such small beam waists presents experimental challenges, particularly at shorter wavelengths. This thesis focuses on the reduction of the beam waist size of a 399 nm probe beam laser in the Ytterbium Non-linear Quantum Optics (Yb-NQO) few photon experiment—hereafter referred to as the main experiment. It aims to study the scattering properties of light interacting with a Yb-Rydberg ensemble.

For this, a replica and test setup was designed to optimize and reduce the size of the probe beam waist, so that the results could be implemented in the main experiment. The work presented here outlines the limitations and challenges encountered during the design setup and the experimental results regarding the reduction of beam size.

Setup of Rydberg Yb experiment

In the following, the setup of the main and test experiment will be explained. Additionally, a quick overview of the goals of the main experiment is presented and why the encountered challenges warrant the effort to even construct a test experiment in the first place.

Furthermore the choice for the key components of the experiment will be elaborated upon and how the experimentation was prepared.

2.1 Main experiment setup

In the main YQO-experiment the goal is to observe non-linear quantum optics by using a 395 nm control laser and a few-photon 399 nm probe laser and shining those onto a Yb-Rydberg ensemble (see Fig. 2.1). The goal is to engage Rydberg transitions by using the control and probe laser, then observing the behavior of that outgoing light to analyze the light-matter interaction. The setup can be seen in Fig. 2.2. The setup is mirrored on each side to provide a higher flexibility, which allows the experimentalists to use co-propagating probe/control beams. The laser beam gets focused by using an achromatic prime lens 1. The choice of this lens will be discussed in Chapter 2.1.3.

To simplify the experiment, the probe beam must be small enough to prepare only single Rydberg atoms in free space. Due to the Rydberg-blockade effect [1], one such Rydberg-atom will prevent another such atom to be created within a certain distance. This distance is called the Rydberg-blockade radius and can be described as

$$r_B = \sqrt[6]{\frac{C_6}{\hbar\Omega_{\text{eff}}}} \tag{2.1}$$

(2.2)

where $\Omega_{\rm eff}$ is the effective Rabi frequency(with $\Omega_{\rm eff} \propto \Omega_{\rm control}^2$) and Δ is the detuning [4]. If the beam waist is $w_0 \leq \frac{1}{2} \cdot r_B$, only single atoms are excited along the beam and thus a chain of Rydberg-atoms will be created, reducing the complexity of the experiment to one dimension.

¹ The prime lens has a focal length of f = 75 mm, a numerical aperture of NA = 0.08 and a visible-nearIR coating by Edmund Optics[3].

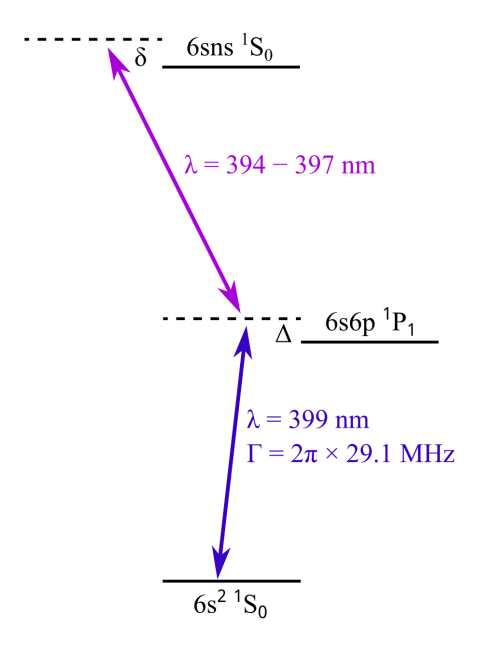


Figure 2.1: Level scheme of the Yb-Rydberg atoms used in the experiment. The probe beam drives from the $6s6s^1S_0$ ground state to the excited state, the control beam will drive from the excited state to the $6sns1_0^S$ Rydberg state, in the YQO experiment a 395 nm laser is used. Image taken from YQO-Lab.

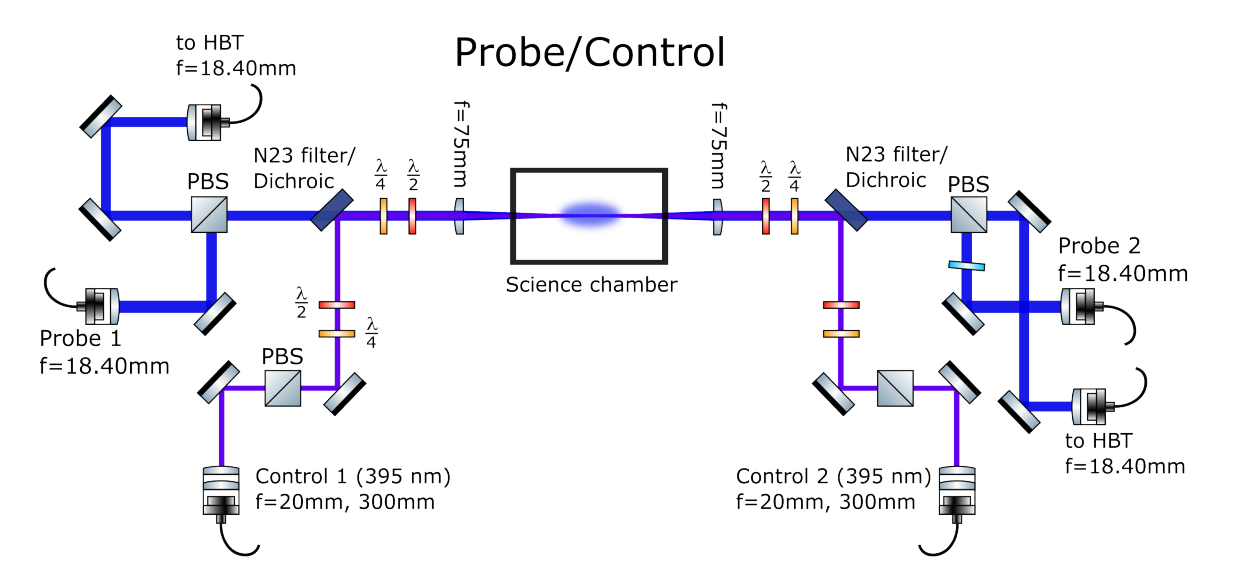


Figure 2.2: Main experiment setup sketch of the optical beam paths of the probe(blue) and control(purple) lasers. Both beams are lead through the science chamber and then recollected on a mirrored side. Image taken from YQO-Lab.

2.1.1 Limitations and goals for testing

The goal of a test setup, is to find out if it is possible to reduce the beam waist to fullfil the requirements so that $r_B \ge 2 \cdot w_0$ holds. The YQO members have provided a calculation, which serves as a motivation for the magnitude of the Rydberg-blockade radius. The calculation is given in Fig. 2.5. As an example of the calculation for the $6s99s^1S_0$ state and an effective Rabi-frequency of 5 MHz, the Rydberg-blockade radius is $8.5 \, \mu m$. Then, the beam waist should be $4.25 \, \mu m$. What waist exactly is aimed for will be elaborated in Section 2.1.3.

A further elaboration of what a Gaussian beam is and what the beam waist refers to is given in Section 2.1.2.

There are a few set parameters which cannot be changed in the main experiment. These parameters should therefore be as closely reproduced as possible in the test setup. These include, the model of the prime lenses—so the type of lens used to focus the beam into the science chamber—the distance between the two glass windows of the science chamber and the length of the beam arms. The length of the beam arms is the least restricted parameter, as the optical elements are in place but could in theory be moved or changed if one would see that it would lead to a significant improvement.

2.1.2 Gaussian Beams

The probe beam is a so called Gaussian Beam, which describes the solution to the paraxial Helmholtz-Equation. The base modal solution can be described by

$$E(\rho, z) = A_0 \frac{w_0}{w(z)} e^{-\frac{\rho^2}{w(z)^2}} e^{ik\frac{\rho^2}{2R(z)}} e^{i(kz - \nu(z))}$$
(2.3)

for a thorough derivation see the textbook by D. Meschede[5]. From this it follows that a Gaussian beam will behave planar-like in the near field, or focal point but spherical-like in the far field. This behavior can be adequately seen in Fig. 2.3. In the figure the beam divergence is described by $\theta_{\rm div}$, the Rayleigh range of the beam by z_0/z_R and the beam size (at its minimal point) with w_0 .

In this thesis the Rayleigh range and the beam size are of particular importance. The Rayleigh range is defined by $z_R = \frac{\pi w_0^2}{\lambda}$ in free space. It parametrizes the distance between where $w(z) = w_0$ and $w(z) = \sqrt{2}w_0[5]$. The point at which the beam size is minimally small, is called the beam waist, which is defined by the condition that $w(z = z_0) = w_0$

The Gaussian beam waist along the z-axis is defined as

$$w(z) = w_0 \sqrt{1 + \left(\frac{z}{z_0}\right)^2}$$
 (2.4)

where z_0 here differs in convention from Fig. 2.3 and is not indicative of the Rayleigh range, but the z-position of w_0 .

If one then shines such a Gaussian beam onto a surface, you would see the intensity distribution of said beam. One such sketch can be seen in Fig. 2.4. The top section shows how the beam itself could look like on the surface, while the graph below shows the intensity distribution. Additionally, here the Gaussian waist is characterized as the so called $1/e^2$ -radius, which is the width of the Gaussian

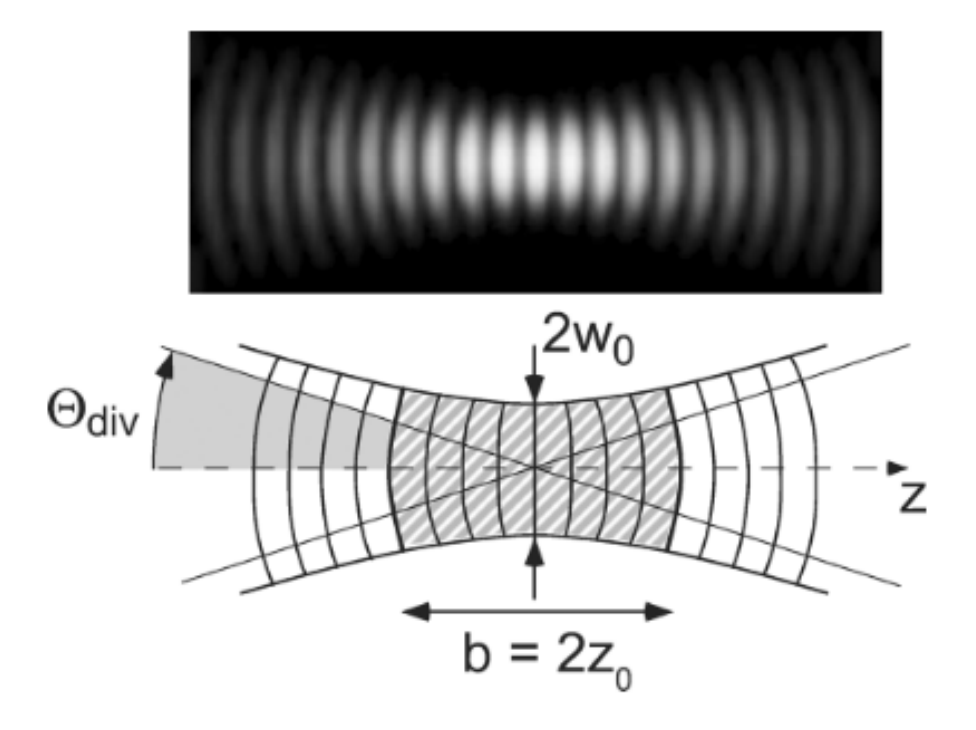


Figure 2.3: Gaussian beam profile along z-axis, here " z_0 " means the Rayleigh range—due to the convention of the used source. Image taken from [5]

intensity distribution which includes 86.5% of the beams intensity.

How to decrease the beam size

In order to reduce the size of the beam one can focus it by using a convex lens. One can manipulate the behavior of this beam waist by carefully choosing the right distance of the z-position of the Gaussian waist w_0 to the lens.

The beam waist of the Gaussian beam after propagating through a convex lens is then:[7]

$$w_0' = \left| \frac{f}{z_0 - f} \right| \cdot \frac{w_0}{\sqrt{1 + \left(\frac{z_R}{z_0 - f}\right)^2}}$$
 (2.5)

where w'_0 is the beam waist after the lens, f is the focal length of the lens, z_0 position of the beam waist and z_R is the Rayleigh length of the beam before the lens. This is a re-written form of the calculation provided by S.A. Self[7].

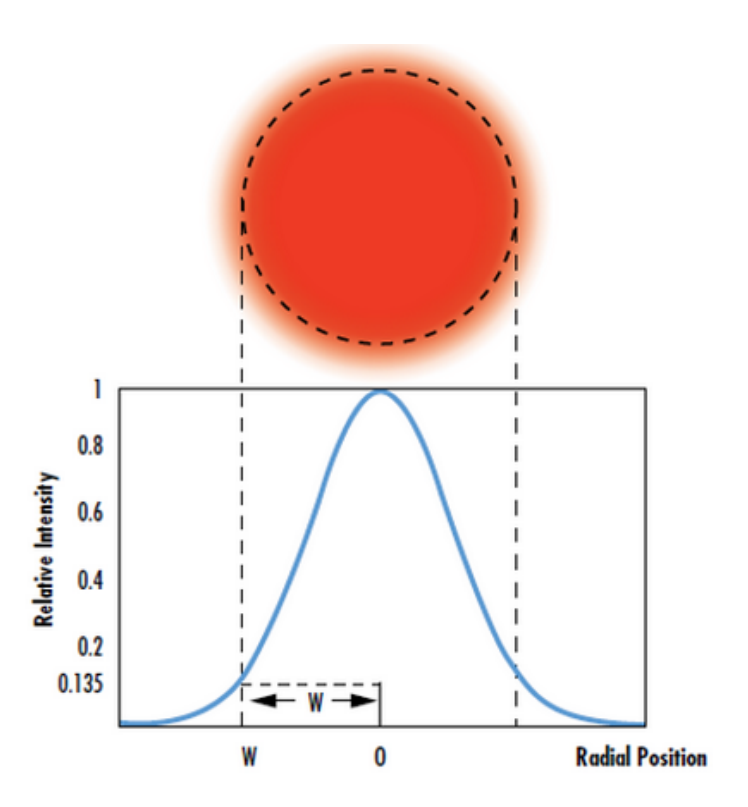


Figure 2.4: Gaussian beam and intensity profile and the corresponding gaussian fit, figure taken from [6].

2.1.3 Choice of lens and collimator

The choice of the proper optical elements is limited by the fact that the beam needs to fullfil the requirement $r_B \ge 2 \cdot w_0$. However, the result of the beam waist after a lens, depends linearly on the already present size before propagating through the lens as given by Eq. 2.5. The Rydberg-blockade radius depends on the effective Rabi frequency, see Eq. 2.1, while the C_6 factor scales with $C_6 \propto n^{11}$ [8]. This means that by carefully choosing the effective Rabi frequency and the target Rydberg state, one can determine the resulting blockade radius and the required beam waist.

For this the YQO-Lab members have previously made a calculation, which was then used to help decide and motivate the parameters of the test experiment. One such example calculation is shown in Fig. 2.5. In the figure, one old beam waist of 8.3 μ m is shown in red, while an estimate for a new beam waist of 5.6 μ m is shown in orange. This already demonstrates the fact, that the right choice of the beam waist will allow the experimentalists to not be forced to drive to such high n-states. In this example, instead of needing to drive the $n \approx 155$ state, a state of only $n \approx 120$ needs to be driven to.

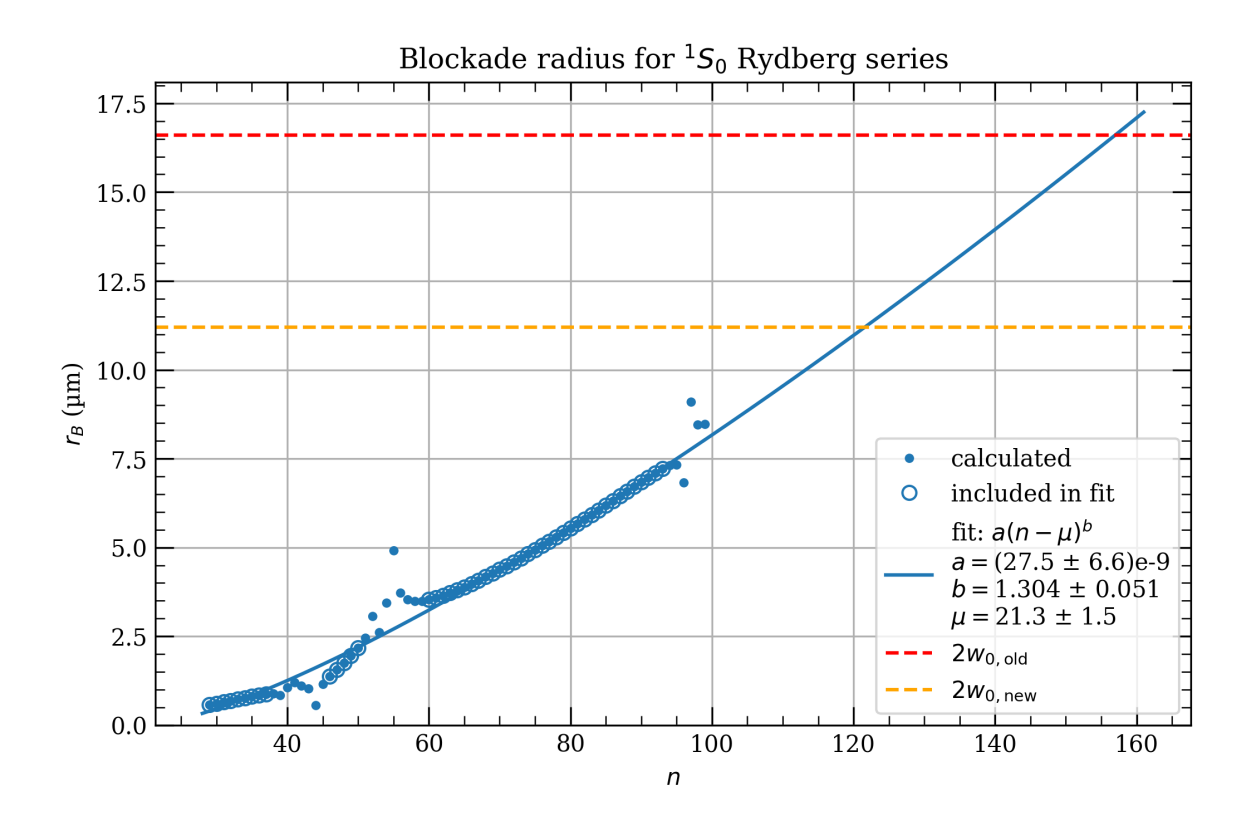


Figure 2.5: Rydberg-blockade radius against principle quantum number n, for $\Omega_{\rm eff}=5\,{\rm Mhz}$. Calculation provided by the YQO-Lab. With $w_{0,{\rm old}}=8.3\,{\rm \mu m}$ and $w_{0,{\rm new}}=5.6\,{\rm \mu m}$. Image taken from YQO-Lab

This is the motivation for why the optical elements were chosen in such a way, so that the resulting new beam waist would roughly be $w_0 \lesssim 6 \,\mu\text{m}$.

Therefore, since the f = 75 mm prime lens has already been chosen and should not be changed, the beam before the lens needed to be adjusted. This is done via using a so called triplet collimator at

the decoupling end of an optical fiber. The triplet collimator is a lens system, that uses three lenses with the goal of creating a well collimated beam at the output. However the manufacturer for the used fiber² does not provide a value for the beam size of the beam exiting the optical fiber.

This means that the beam size before the collimator is not known, which complicates the choice of the right collimator. So the following approach was taken: a collimator whose mode-field-diameter (MFD) was roughly known, was chosen and the resulting outgoing beam was measured using a beam profiler. Then the beam divergence angle is described by[5],

$$\theta = \lim_{z \to \infty} \arctan\left(\frac{w(z)}{z}\right)$$

which in the paraxial case can be approximated to

$$\theta = \frac{\lambda}{\pi w_0}$$
 , in free space. (2.6)

Then since a single-mode fiber is used in the experiment, the collimated beams waist can be written as [10]

$$w_{\text{collimated}} = f \cdot \theta \approx \frac{f \cdot \lambda}{\pi w_{\text{fiber}}}$$
 (2.7)

where f is the focal length of a lens (in this case the triplet collimator), where λ is the wavelength and w_{fiber} is the beam waist of the laser beam inside the fiber. The beam profile that was taken can be seen in the Appendix A.3(b), from there one can find that the beam waist of the collimated beam is roughly $w_{\text{collimated}} \approx 1.541 \text{ mm}^3$. The triplet collimator that was used has an effective focal length of 24.765 mm for the used wavelength of $\lambda = 399 \text{ nm}^4$. This leads to a MFD—the size of the exiting fiber— of

MFD =
$$2 \cdot w_{\text{fiber}} = 2 \cdot \frac{24.765 \text{ mm} \cdot 399 \text{ nm}}{\pi \cdot 1.541 \text{ mm}} \approx 4.082 \,\mu\text{m}$$
 (2.8)

an example of how the beam looks along the path can be found in the following section in Fig. 2.6

Simulation

To check if this collimator is a good choice for the test experiment, the calculated MFD from Eq. 2.8 is used to calculate the final focused beam waist after the prime lens. For this it needs to be considered that the prime lens also experiences a wavelength-dependent focal length shift of around 180 µm[3]. Additionally a simulation is done, by a program which follows the same equations, using the program is a healthy crosscheck to realize if any measured values are significantly different from what they should be.

² Model QPMJ-3A3A-400-3/125-3-5-1[9]

³ This is the value of the effective diameter of the beam profile.

⁴ Information taken from Thorlabs Inc. TC25APC-405 405 nm Triplet Fiber-Optic Collimator Datasheet-collimator-thorlabsTC25APC405, https://www.thorlabs.com/thorproduct.cfm?partnumber=TC25APC-405 The manufacturer does not provide a focal length for a wavelength of 399 nm, thus the data table provided on the website was used to extrapolate and calculate an estimation for the desired wavelength manually, more details about this in the Appendix A.4

Optics	Position (mm)	Relative position (mm)	Properties	Waist (μm)	Waist position (mm)	Rayleigh range (mm)	Divergence (mrad)	Sensitivity (%/mm²)	Name	Lock
Input be	0		n = 1, M ²	2.04	0	0.032767	62.1774	23279	w0	absol
Lens	24.77	24.77	f = 24.76	1474.37	5272.91	17115.5	0.0861424	23279.1	L1	none
Lens	274.77	250	f = 74.82	6.17945	349.501	0.300661	20.55	276.565	L2	none

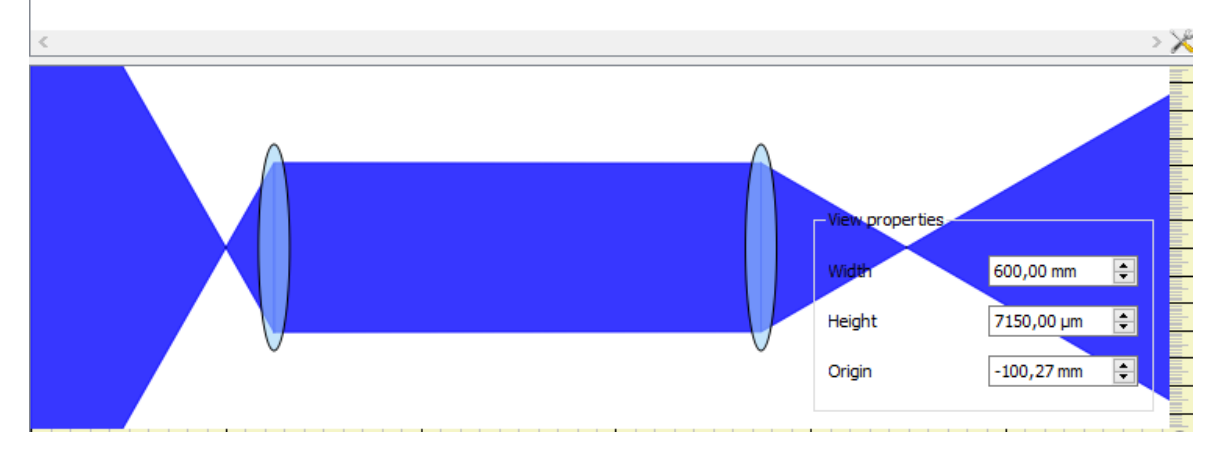


Figure 2.6: Screenshot of a simulation program which calculates a 399 nm laser beam propagating through two lenses. The first lens has a focal length of 24.76 mm (triplet collimator, left) and the second lens a focal length of 74.82 mm (prime lens adjusted for wavelength focal shift, right). The simulation assumes a MFD of 4.08 μ m (left minimal point) and predicts a final beam waist of $\approx 6.179 \, \mu$ m (right minimal point). The text box at the bottom right, is simply used to scale the simulation picture for better visualization.

Then using Eq. 2.5 the final beam waist can be calculated to

$$w'_0(f = 74.82 \,\text{mm}, \, w_0 = 1.541 \,\text{mm}, \, z_0 \approx 0) = 6.166 \,\mu\text{m}$$
 (2.9)

Thus, a beam waist of $6.166 \, \mu m$ from the calculation (in line with the simulation of $\approx 6.179 \, \mu m$) is assumed to be the "ideal value". Keeping in mind that this value is a very rough estimation, rather than an accurate prediction, due to the uncertainties and ambiguity of the MFD and collimated beam waist.

2.2 Test Setup for Probe Beam Waist Optimization

2.2.1 Used components

With the correct choice of the lens and triplet collimator, the test experiment could be set up. In Fig. 2.7 a sketch of the experiment setup can be seen. An actual photograph of the test setup can be found in Fig. 2.8. In the setup, the 399 nm probe beam is first lead through some ND Filters to attenuate it, then it is coupled into an optical single mode fiber. If this would not be done, the high intensity of the beam could damage the camera that is used for measuring the probe beam. Then, from the other end of the fiber, the f = 25 mm triplet collimator is used to to create a collimated beam.

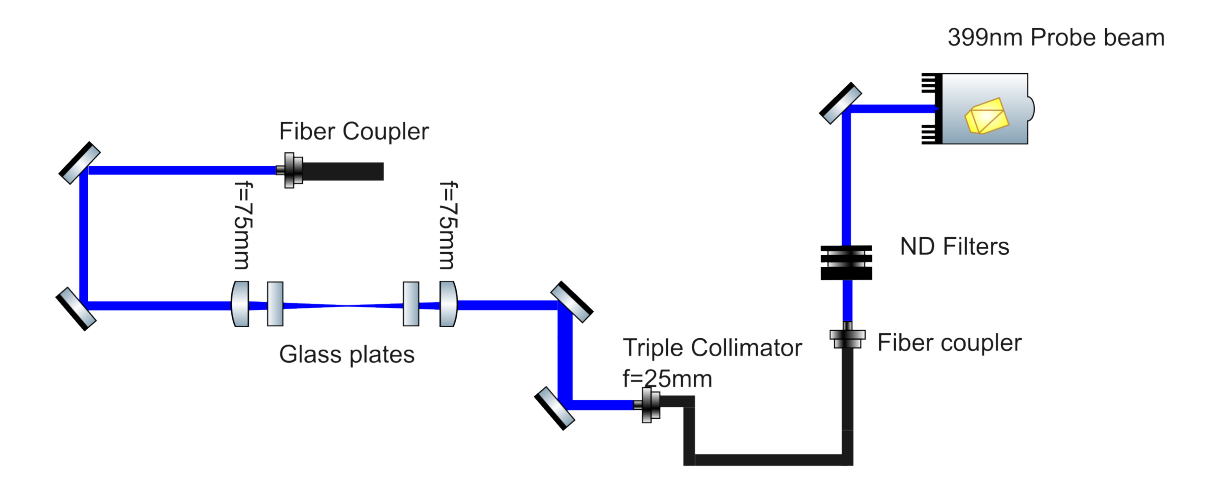


Figure 2.7: Test setup sketch to simulate main experiment. The beam is lead through ND filters to reduce the intensity of the beam onto the camera and prevent any damage, but also not reduced too low, to lose a good signal to noise ratio. Afterwards, the beam is coupled into a fiber, collimated with a triplet collimator[11] and then focused by an achromatic lens[3] with a focal length of 75 mm. After passing the glass plates, the focused beam is re-collimated by a second lens of the same kind and then coupled back into a second fiber. Both fiber couplers are mounted on optical mounts and have the same triplet collimator[11].

It is important that the beam is well collimated, to ensure a high optical beam quality. A divergent beam could lead to clipping losses during the rest of the beam path and would cause the beam to not be focused at the focal point of the lens. Then the beam can be lead to propagate to get focused by a lens and is then lead through a glass plate. The glass plates are used to simulate the science chamber windows.

The realization of this construction came with two challenges. Firstly, a lens mount needed to be engineered, which would allow for a fine adjustment along the z-axis parallel to the beam. The custom mount should also allow to not just focus the beam, but to also closely adjust the position of the lens so that the smallest beam waist can be achieved. Secondly, a glass plate-holder was needed, to actually allow the beam to propagate through it.

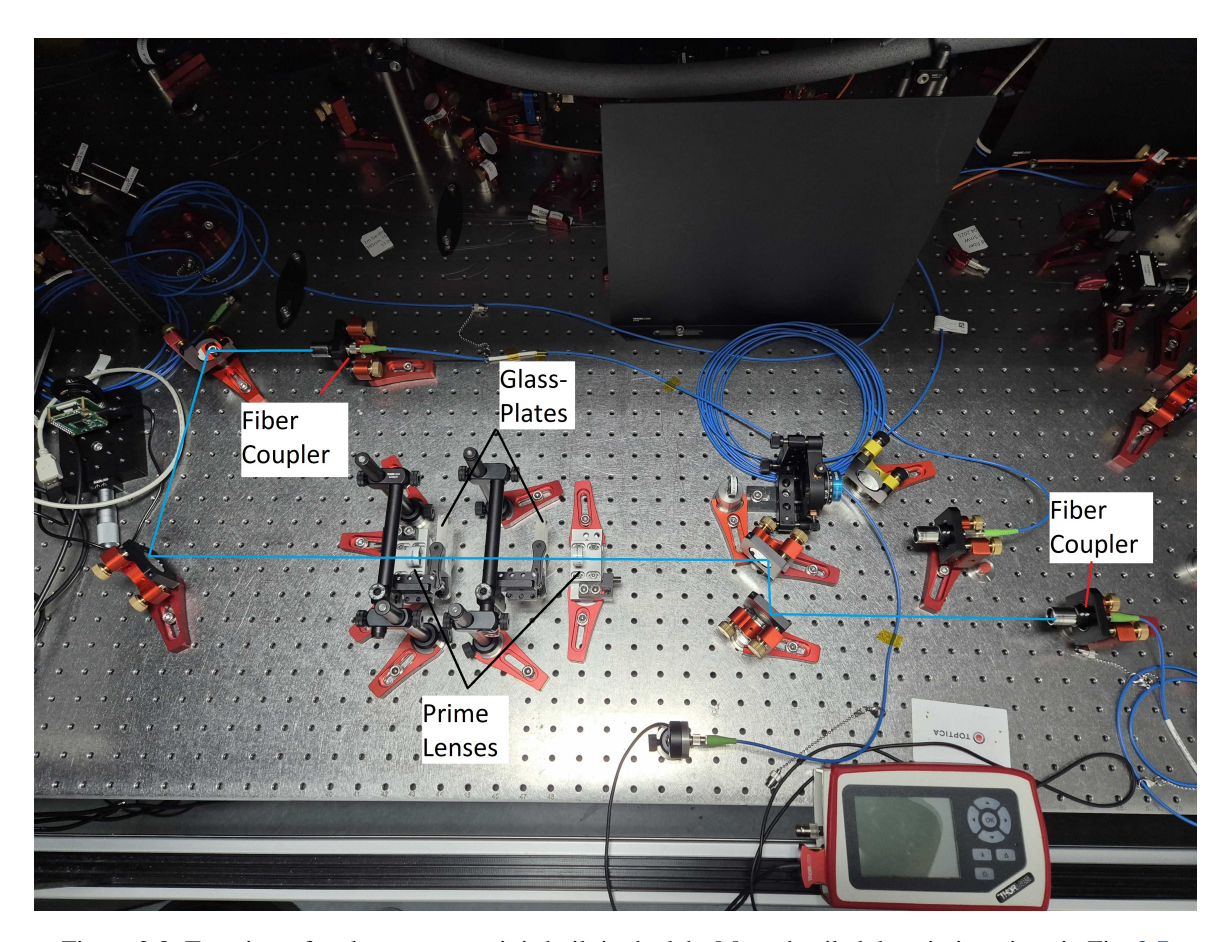


Figure 2.8: Top view of real test setup as it is built in the lab. More detailed description given in Fig. 2.7

Lens mount

For the lens mounts, a construction was designed that would allow for the aforementioned z-axis positional adjustment. An image of this custom lens mount can be seen in Fig. 2.9.

The lens will be mounted on a lens-holder which itself is mounted on a z-axis translation stage, which can be finely adjusted with micrometer precision. To guarantee the the lens mount is not angled, a groove is cut into the translation stage and the lens is screwed in from the bottom of the stage. Therefore, the lens mount can only be fully screwed in if it is aligned to the grove, which in turn makes sure that the lens is not angled. This exact design for the mount was chosen, as the same mount is already built into the experiment, using this design allows for an accurate reproduction of the results of this thesis.

Glass plate holder

For the glass plates an assortment of mechanical pieces were used to salvage together a solution to hold the glass plates at the height of the laser, while avoiding that the glass would touch any metal pieces or objects. As can be seen in Fig. 2.11 two mechanical pieces with rubber tips hold the glass plates in place.



Figure 2.9: Custom designed lens mount, with lens holder on a z-axis translation stage with micrometer precision adjustment screw tool. Image taken from YQO-Lab

Camera placement

As a note, the camera that was used⁵, to analyze the beam waists, is placed behind the first glass-lens pair. The camera was on a z-axis variable translation stage, as seen in Fig. 2.10, which allowed for micro-meter adjustments in identifying the beam waist position. Such precision is needed, since the Rayleigh-range for a $w_0 = 6.166 \,\mu\text{m}$ and wavelength of 399 nm is $z_R = 299 \,\mu\text{m}$. For how the alignment of the beam through the lens (and glass) is done, see Chapter 2.2.2.

Second lens-glass pair

After the focused beam, another pair of glass plate and lens is positioned. Here the distance between the glass plates was chosen, so that it would match the distance between the windows of the science chamber in the main experiment, which is about 103 mm. The position of the second lens, needed to be adjusted in such a way that the outgoing beam is well collimated again.

Second fiber coupler

In order to observe the collection efficiency, the beam is coupled into a fiber again. This allows for a quantification on how much the optical elements deteriorate the wavefront.

⁵ ArduCAM CMOS MT9J001 1/2.3 10 MP Monochrome Camera Module, pixel size of 1.67 μm × 1.67 mm, from now on this camera model will only be referred to as "the camera" https://www.arducam.com/arducam-cmos-mt9j001-1-2-3-inch-10mp-monochrome-camera-module.html

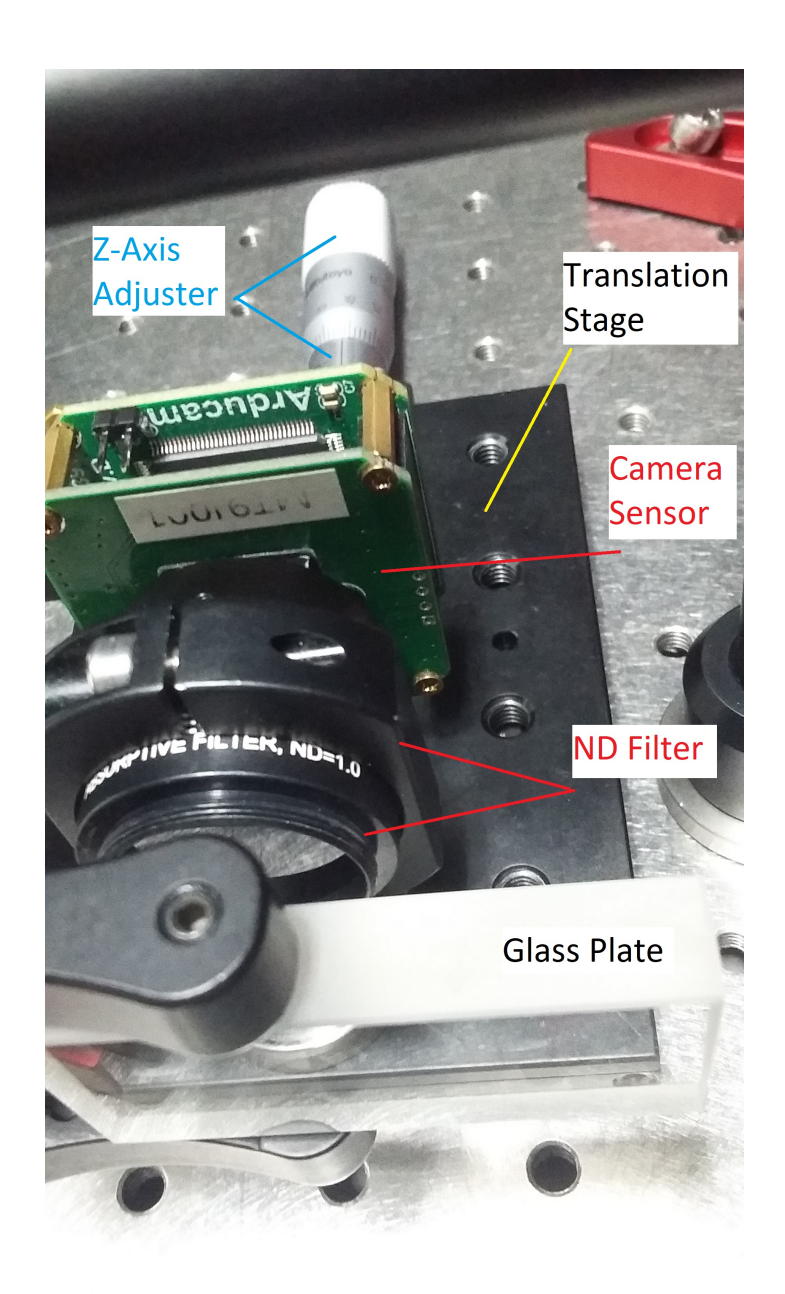


Figure 2.10: Picture taken of the camera on a z-axis translation stage, which allows for micro-meter adjustments in identifying the beam waist position. With the glass plate and ND filter visible too.

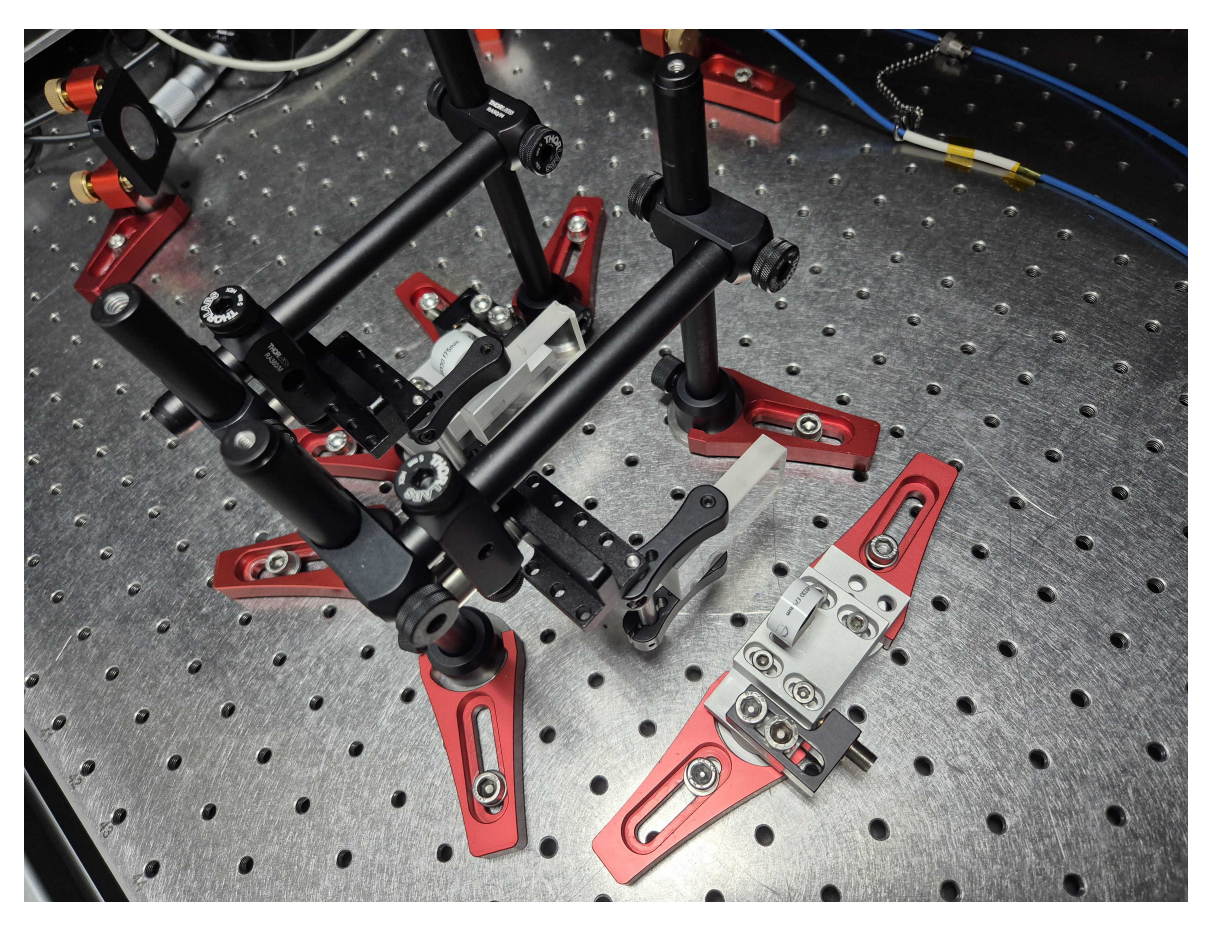


Figure 2.11: Custom built mirror-holders to hold the glass plate in place. Two mechanical pieces, hold the the glass plates with rubber tips to avoid any damages. Beam propagates roughly through the vertical center of the glass plates.

2.2.2 Alignment strategy

The alignment of the different type of optical elements each require a certain finesse. Therefore, some of the used methods and concepts for alignment will be discussed here. Certain experimental limitations or problems and how they were handled are also mentioned here.

Mirror Alignment + Fiber Coupling

In order to couple the laser into an optical fiber a method known as "hill climbing" is used—when only working with mirrors it is often called "beam walking"—which is outlined in more detail here [12]. When using only mirrors to align a laser the same steps are followed, except two irises are used as targets instead of a fiber. In order to quickly elaborate on this method, the following steps are followed in order to find the highest coupling efficiency;

- 1. Align the laser to have a signal of whatever strength. For this, a fiber-coupled laser pen can be used to emit light from the fiber, allowing alignment of the probe beam to match the path of the laser pen beam
- 2. Since the optical fibers in the test experiment are built into optical mounts, it is possible to use mirrors for coarse alignment, and the fiber mounts for fine alignment.
- 3. Start the "hill climbing" algorithm.
 - a) Begin by choosing an angle to optimize, either the pitch or yaw.
 - b) Turn the coarse alignment either clockwise (CW) or counter-clockwise (CCW)
 - c) Attempt to couple a stronger signal by turning the fine alignment either way
 - i. If a stronger signal can be coupled, repeat steps b)(in the same direction) and c)
 - ii. If no stronger signal can be coupled, repeat steps b)(in the opposite direction) and c)
 - iii. If the highest possible signal has been coupled, optimize the other angle
 - d) Repeat steps a) to c) until global maximum has been coupled. In case the absolute peak (see Fig. 2.12) seems to have been reached, but it is only a low efficiency (usually less then 10%) either begin again with a better alignment (step 1), or a few iterations of step b), skipping step c).

Aligning laser through lens

The custom built lens mount (Fig. 2.9) allows for careful z-axis adjustments, where the z-axis describes the propagation axis of the laser beam, but x-y-axis adjustments, so the horizontal and vertical axis perpendicular to the beam propagation axis, need to be done by hand. It should be noted, that the construction is normalized such that, the beam height is always 50 mm, this serves as a coarse alignment. Mirrors are then used to fine tune on micrometer scale.

In order to achieve the highest beam quality, the probe beam needs to go through the center of the lens. This can be checked by two methods, first one can use a piece of paper for example and hold it right behind the lens to get a rough estimation on how well the beam is hitting the center of the lens. Another much more detailed, but also time-consuming way is to change the lens' z-position after the

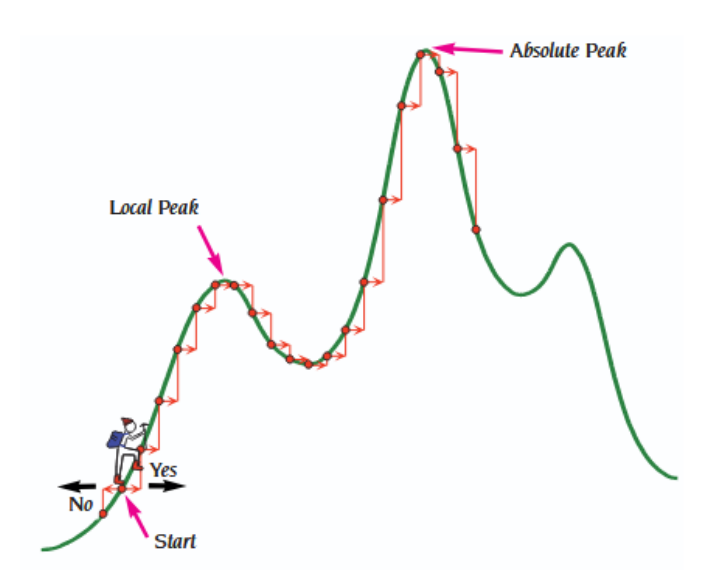


Figure 2.12: Symbolic image of "hill climbing" algorithm and a local and absolute peak. Image taken form [12]

x-y position has been set. If the beam x-y position changes, when the lens' z-position is changed, then the beam is not going perfectly through the center of the lens. If the beam does not change in x-y position, even after changing the z-position of the lens, then beam is hitting the center of the lens.

Re-collimating the focused beam

After the beam has been focused, it needs to be re-collimated, in order to be coupled back into an optical fiber. This re-collimation was done by using the second lens. In order to collimate the focused beam, the second lens needs to be exactly at the effective focal length away from beam waist position. However as later discussed in Chapter 3.2, the focal point will shift due to the glass plate, which will need to be accounted for when positioning the second lens. This needs to be done, while the distance between the glass plates is not changed, so that they maintain the distance of the windows of the main experiments science chamber. The collimation of the beam was then checked by using a shear-plate interferometer.

Test Experiment Methods and Results

In this chapter, the methods used and the results of the test experiment are presented. The focus lies on how the beam waist was measured, what final beam size was achieved, and how the windows of the science chamber in the main experiment might influence the laser beam. In particular, this includes a description of the camera calibration process and the procedure used to extract beam waist values from the recorded images.

3.1 Achieved waist and used strategy

3.1.1 Presentation of Calibration Strategy

Firstly, it will be discussed how the images were taken and prepared to measure the beam waist of the laser at different z-axis positions. All images were taken by using a camera¹. The code for taking the images with the camera was prepared by Samuel Germer, a more detailed discussion on the production of this code can be read in his Bachelors Thesis [13].

During initial testing, issues arose when analyzing the images directly. In particular, artifacts resembling a "checkerboard" Bayer pattern [14, 15] were observed, which introduced significant errors in beam waist calculations. These artifacts would generally stem from an improper calibration of the gain settings for the different color channels. This mismatch between pixels manifests as spatial variations in brightness and color in the raw image as can be seen in Fig. 3.1(b). During experimentation, and even after the pixel gain settings had already been properly calibrated by Samuel Germer [13], such artifacts were still present. Several factors could have contributed to this issue, like an improper analog to digital conversion, however it was not fully determined what exactly caused this and the ultimate solution was to used a different camera of the same model. Then, calibration procedure was implemented to compensate for the differing gains across pixel types. The method of this calibration, along with its effectiveness, is detailed below and illustrated in Fig. 3.1.

All the following errors regarding the pixel value for each individual pixel, which is an arbitrary unit by the camera proportional to the amount of photons per camera frame, follow a Poisson-distribution, $\Delta N = \sqrt{N}$ due to the nature of photon-matter interaction [16]. For errors regarding

¹ ArduCAM CMOS MT9J001 1/2.3 10 MP Monochrome Camera Module, pixel size of 1.67 μm × 1.67 mm, https://www.arducam.com/arducam-cmos-mt9j001-1-2-3-inch-10mp-monochrome-camera-module.html

mean values, the approach is taken to maintain the poissonic nature of individual pixel while accurately describing mean value error propagating, leading to the fact that they will be calculated via $\Delta N = \sqrt{N}/\sqrt{\text{number of pixels}}$.

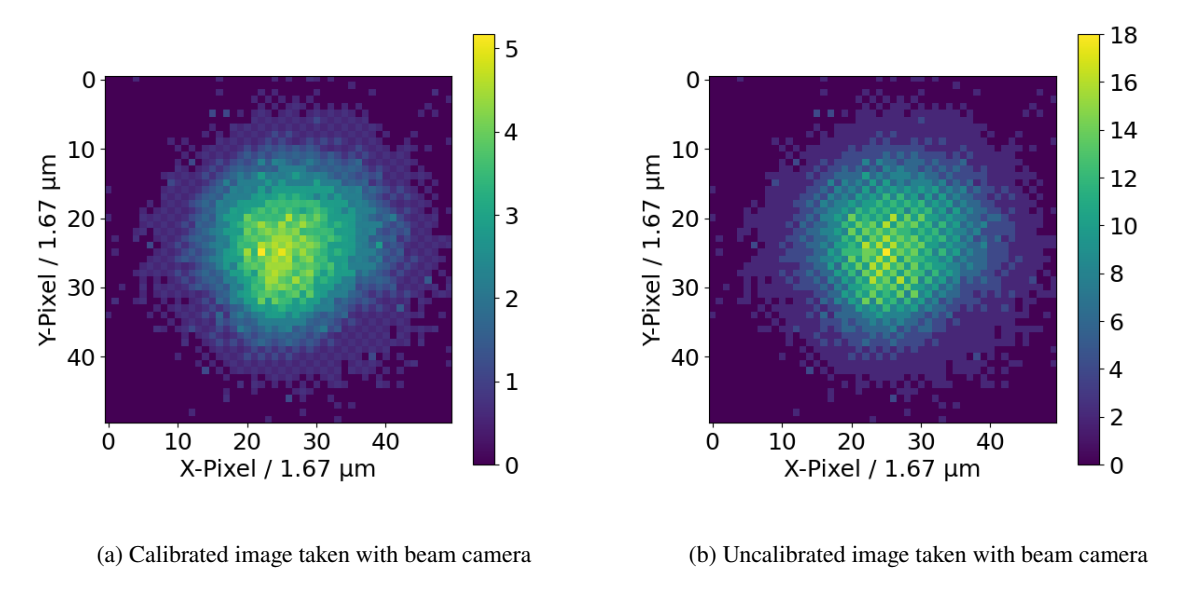


Figure 3.1: Uncalibrated (right) and calibrated (left) image taken with the same camera as outlined above. Checkerboard Bayer-pattern can be seen in the uncalibrated image.

In order to calibrate the images, a method is used that can be viewed on the flowchart in Fig. 3.2. A more detailed explanation is given here;

- Measure dark count images, prevent any signal of reaching the camera pixels
- Create a homogeneously illuminating beam that shines on the entire pixel range using a divergent lens at different exposure times, optimally covering the entire exposure time range
- Take a set of raw camera data, which takes beam profile images at different z-axis positions of the camera relative to the lens, which allows a fine and detailed analysis of the beam waist position and size
 - 1. Subtract the dark count images from the homogeneous images
 - 2. Calculate the average of each pixel type. Ideally each pixel of each type should have the same value due to the homogeneously illuminating beam. This is done once along the x-axis (x-scan) and along the y-axis (y-scan). Here the distinction allows to spot any systematic errors in the camera, like every second row having a different gain setting.
 - 3. Plot the average of each pixel type against the exposure time range
 - 4. Create a linear fit, extracting the slope and intercept. Since the dark images were subtracted, the intercept should ideally be at zero
- Subtract the dark count images from the raw beam profile data

• Divide each pixel type by the slope of the corresponding pixel type linear fit (scaling factor), so that the Bayer pattern can be mostly eliminated (see Fig. 3.1 as reference)

The linear fit that was used for the extraction of the scaling factors can be seen in Fig. 3.3. This calibration serves the purpose of eliminating the Bayer pattern. If the pattern were to remain, it would introduce false spatial modulation and would thus falsify the analysis of the beam waist.

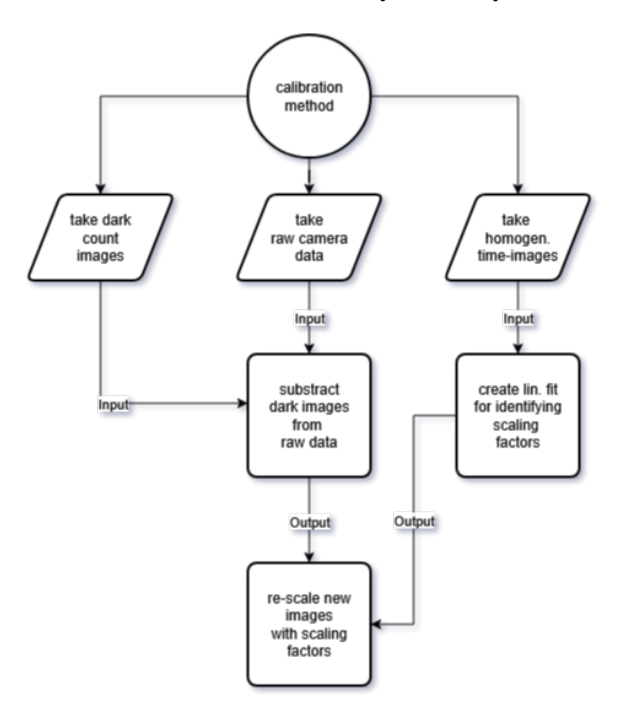


Figure 3.2: Camera image calibration method flowchart

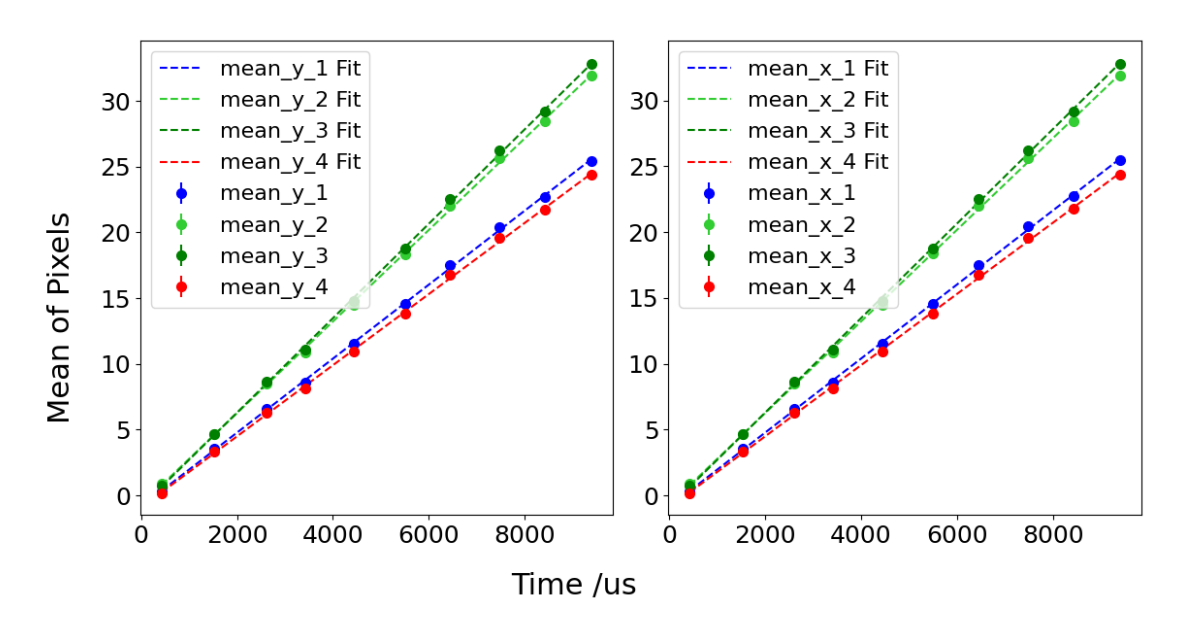


Figure 3.3: Linear fits used for extracting the scaling factors, for the y-scan (left) and x-scan (right). Data points are the mean values of the x,- and y-scanned sums of the homogeneously illuminating beam against different exposure times, covering the range of the camera. Errors are calculated by taking the Poisson-error distribution into account, so taking $\Delta N = \sqrt{N}/\sqrt{\text{number of pixels}}$. Since both scans are almost identical, there seems to be no systematic error in the pixel gain settings.

3.1.2 Presentation of analysis strategy

The measurements here are taken by placing the camera behind the prime lens. For this measurement no glass plate is placed along the beam path. In order to actually measure the beam profiles/widths with the camera, the camera was positioned in such a way, that for the highest exposure time, the beam was nearly un-distinguishable from the light noise. Then, the camera was moved along the translation stage towards the focal point and a bitmap was taken of the captured camera image. This process was repeated until the focal point was reached, afterwards the camera would be moved away from the focal point until the beam was again nearly un-distinguishable from the noise. This determined the z-axis range that was taken. It should be noted that the translation stage allows for a z-axis range of about 25 mm, however here only a fraction of that was used, around 2 mm.

With the calibrated images produced with the method shown in Chapter 3.1 the beam waists can be extracted. The flowchart in Fig. 3.4 outlines the used method, a more detailed explanation on how the beam waists were extracted is given below;

- From the calibrated images, the pixel values for each pixel type are summed. If the beam would be perfectly circular, the x- and y-scans would have the same results. If there is a discrepancy, then the beam has an ellipticity $\epsilon \neq 1$ or an astigmatism caused by inproper beam alignment. These effects would be caught by comparing the x- and y-scans.
- These sums will follow a Gaussian distribution thus allowing a characterization by using a Gaussian fit model. The exact model used is outlined in Section 3.1.3
- From the Gaussian fit's width, the $1/e^2$ -waist is extracted
- For each z-position beam profile, the beam waist is plotted against the respective z-position

As a reminder, the z-position of the camera is somewhat arbitrary, since the numerical value of the z-position simply reflects the setting of the translation stage. However, the difference in distances is what allows a proper analysis. So even though the focal length of the lens is 75 mm the beam waist will not be found at a z = 75 mm of the camera. This is an important detail when trying to quantify the beam waist shift. So in order to accurately represent the beam waist shift (see Chapter 3.2), neither the camera on the translation stage, nor the lens were moved in between the measurements with and without the beam propagating through a glass plate.

3.1.3 Gaussian Fit model

All Gaussian fits are produced using a Gaussian fit model. This fit model is described by the following formula,

$$f(x) = A \cdot e^{-(x-\mu)^2/\left(2 \cdot \sigma^2\right)}$$
(3.1)

where A is the amplitude, μ the mean, σ the standard deviation, the $1/e^2$ value is calculated from the σ by width_{$1/e^2$} = 0.848 · FWHM [17]. The previously shown Fig. 2.4 shows again how $1/e^2$ is identified in an Gaussian fit.

Additionally, an example of the actual measurements similar to Fig. 2.4 is given in Fig. 3.5 to help visualize the procedure.

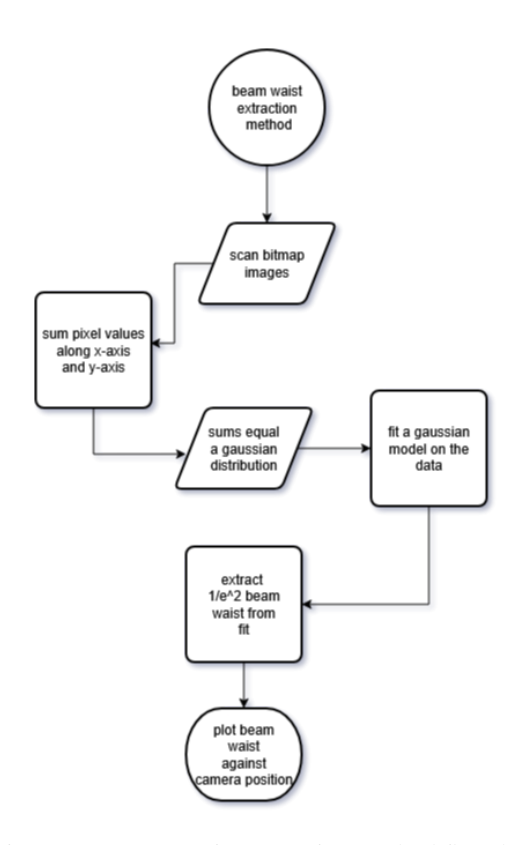


Figure 3.4: Beam waist extraction method flowchart

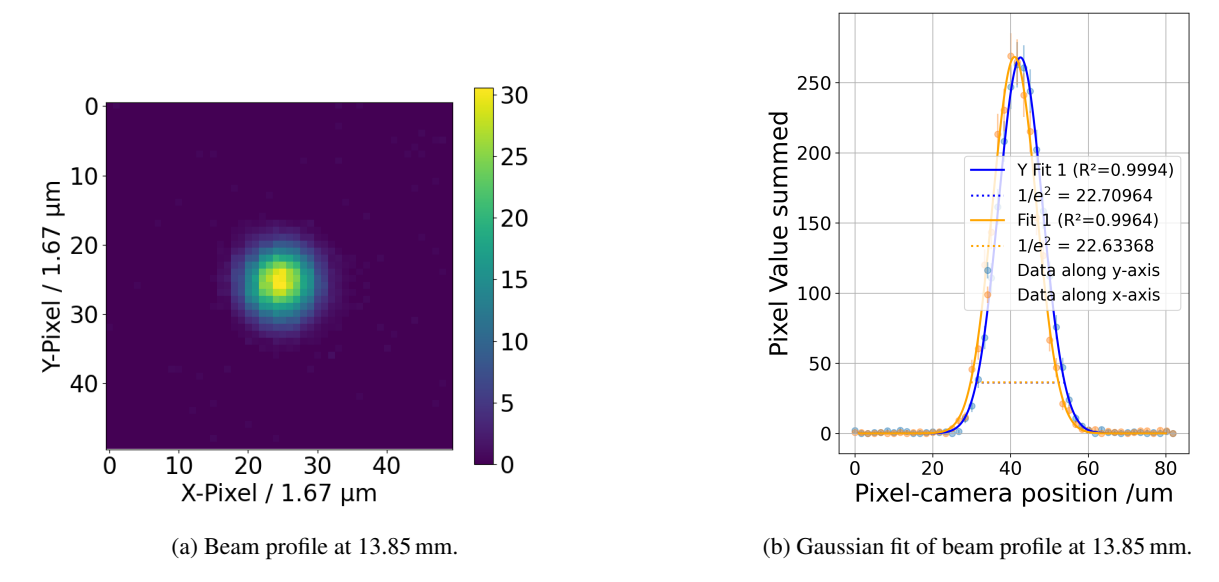


Figure 3.5: Beam image and corresponding Gaussian fit 3.1 at 13.85 mm (no glass). The Gaussian fit in Fig. 3.5(b) shows a dotted line, which is at the position of the $1/e^2$ width, for both fits the quality factor R^2 shows how well the fit fits to the data, ideally $R^2 = 1$. This z-position was chosen to for no particular reason other then being clearly visible.

3.1.4 Presentation of measurement results

As a reminder, the goal is to determine whether a beam waist can be achieved that matches the theoretical prediction given in Section 2.1.1, specifically Eq. 2.9. To test this, the 399 nm probe beam is focused using the achromatic lens and directed onto the camera. By moving the camera along the z-axis using the translation stage, the beam profile can be measured at different positions. This allows for precise identification of both the beam waist location and its minimum size.

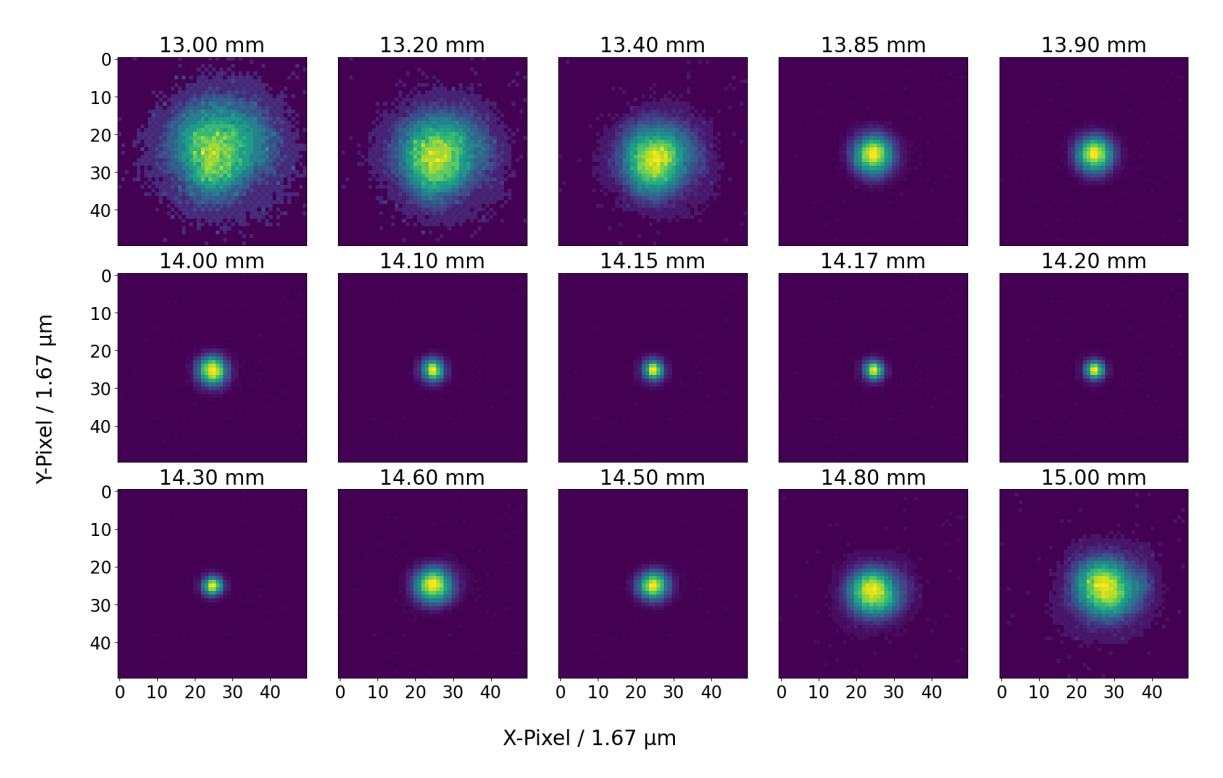


Figure 3.6: Beam profile evolution along propagation axis at increasing z-positions from 13.0 mm (first image of measurement) to 15.0 mm (last image of measurement), no glass in the beam path. Each image uses a relative color scale, which shows the camera pixel value, after calibration. Each pixel has a size of $1.67 \, \mu m \times 1.67 \, \mu m$. The axis show the pixel position of the beam on the camera, the image is automatically centered to the brightest point of the beam.

The camera data of the beam width progression after calibration can be seen in Fig. 3.6. One can see how the beam width shrinks and then enlarges again. Also the integral-normalization in Fig. 3.7, allows to see any intensity asymmetries which might be caused by an incorrect alignment. In the figure no strong asymmetries, can be observed. The vertical lines near the beam waist/focal point are artifacts from the integral-normalization and bear no further physical meaning. In an maximum-value normalization scheme, the beam waist should show as being the most intense.

The respective Gaussian fits can be viewed in the Appendix A.1.

As previously described the method used to identify the smallest achieved beam waist (Fig. 3.4), produces a w(z) against z plot. To produce a fit to characterize this behavior two different fitting

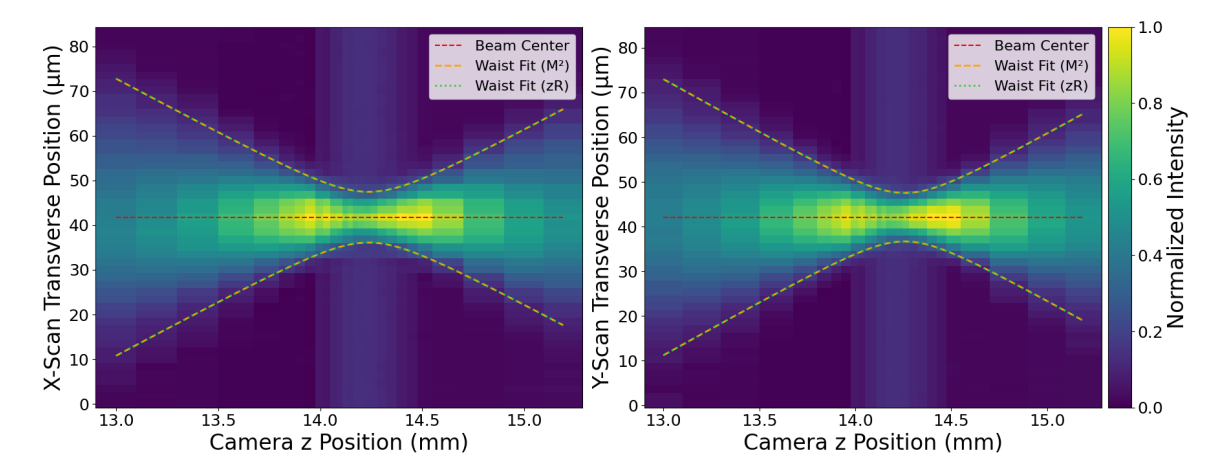


Figure 3.7: Beam width evolution along z-axis, no glass plate in beam path. Showing the transverse position, of the beam profile at different z-positions with a integral-normalized intensity color scale. Fits from Fig. 3.8 are inserted.

models are used. First the Fixed z_R -parameter fit which takes the following form:

$$w(z, w_0, z_0, M^2) = w_0 \sqrt{1 + M^2 \cdot \left(\frac{z - z_0}{\pi w_0^2 / \lambda}\right)^2}$$
(3.2)

where w_0 is the beam waist, z_0 is the position of the beam waist, \textbf{M}^2 is the beam quality factor and λ is the wavelength of the laser light.

Here a new parameter is mentioned, the beam quality factor M^2 [18], this is a parameter which allows to quantify how gaussian a Gaussian distribution is. This beam quality factor describes the ratio between the beam's actual waist-divergence product and that of an ideal diffraction-limited Gaussian beam. For an ideal Gaussian beam (where $M^2 = 1$), the beam waist is as small as physically possible for a given divergence angle θ . This means the beam is perfectly focused and free of distortions or aberrations. It can be defined by adjusting Eq. 2.6 to [18]

$$M^2 = \frac{\theta \cdot w_0 \cdot \pi}{\lambda} \tag{3.3}$$

a small intuition on how the beam quality factor impacts the beam is given in the Appendix A.3. In the z_R -parameter model the Rayleigh range is explicitly written out and therefore dependent on w_0 . This is different in the other fitting model. The Fixed M^2 -parameter fitting function leaves the Rayleigh range as an additional free parameter

$$w(z, w_0, z_0, z_R) = w_0 \sqrt{1 + \left(\frac{z - z_0}{z_R}\right)^2}$$
with $z_R = \frac{1}{M^2} \frac{\pi w_0^2}{\lambda}$ (3.5)

with
$$z_R = \frac{1}{M^2} \frac{\pi w_0^2}{\lambda}$$
 (3.5)

In theory, both models should return the same values since they are simply shifting the degree of freedom from one parameter to the other. But comparing the fitted M^2 value and then one calculated from Eq. 3.5 allows a consistency-check.

In addition, another consistency-check is introduced into the fit-plots, a red "simulated" plot is shown. This simulated plot serves as a reference between all w(z) vs. z plots, as the red fit is always the same. It is made by using Eq. 3.5 with the following fixed values taken from the earlier calculation (Eq. 2.9);

$$w_0 = 6.166 \,\mu\text{m}$$

$$\lambda = 399 \,\text{nm}$$

$$z_R = \frac{\pi w_0^2}{\lambda} = 0.299 \,\text{mm}$$

$$M^2 = 1$$

with this reference, changes in the fit-behavior can be easily visually compared. The offset z_0 is set to be the same as the one for the y-scan Fix z_R -parameter fit in all figures.

The extracted $1/e^2$ -waists from the Gaussian fits A.1, are then plotted against their z-positions, the result and the fit parameters can be found in Tab. 3.1. An alternative way to visualize the beam waists and the z-positions, is by plotting the transverse position- or beam width in a color map like in Fig. 3.7.

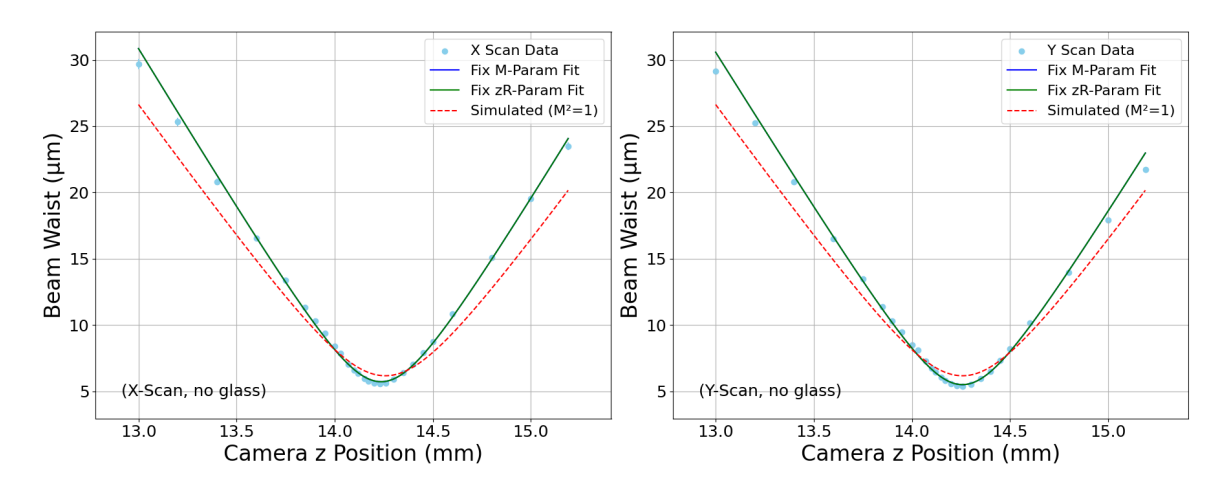


Figure 3.8: Beam width against z-position fits. The beam is not propagating through a glass plate. Fit-parameters are listed in tab. 3.1, fitting models used are Eq. 3.2 and Eq. 3.4. The red line is the simulated fit, which is the same for all figures in this chapter. The beam width data is extracted from the beam profile images in Fig. 3.6. The x-axis shows the z-position of the camera, which is arbitrary, but the difference in z-positions is what matters.

Converting the Rayleigh lengths to an a M^2 value, we find using relative error propagation

$$z_{R,x-\text{scan}} = (0.233 \pm 0.003) \text{ mm} \implies M^2 = \frac{\pi \left((5.72 \pm 0.05) \,\mu\text{m} \right)^2}{(0.233 \pm 0.003) \,\text{mm} \cdot 399 \,\text{nm}} \approx 1.105 \pm 0.024 \quad (3.6)$$

$$z_{R,y\text{-scan}} = (0.224 \pm 0.001) \text{ mm} \implies M^2 = \frac{\pi \left((5.42 \pm 0.01) \, \mu\text{m} \right)^2}{(0.224 \pm 0.001) \, \text{mm} \cdot 399 \, \text{nm}} \approx 1.036 \pm 0.006 \quad (3.7)$$

Axis	Fit Type	<i>w</i> ₀ [μm]	z_R [mm]	<i>z</i> ₀ [mm]	M^2
X	Fixed z_R -Param Fit Fixed M^2 -Param Fit Simulated (M^2 =1)	5.72 ± 0.05 5.72 ± 0.05 5.577	$ \begin{array}{c} - \\ 0.233 \pm 0.003 \\ 0.245 \end{array} $	14.237 ± 0.002 14.237 ± 0.002 14.257	1.104 ± 0.006 - 1.000
Y	Fixed z_R -Param Fit Fixed M^2 -Param Fit Simulated (M^2 =1)	5.50 ± 0.01 5.50 ± 0.01 5.577	-0.230 ± 0.001 0.245	14.258 ± 0.001 14.258 ± 0.001 14.257	1.035 ± 0.002 - 1.000

Table 3.1: Beam waist fit results for X and Y scans and simulation.

So the values from the Fixed z_R -model ($M_{\text{x-scan}}^2 = 1.104 \pm 0.009$ and $M_{\text{y-scan}}^2 = 1.035 \pm 0.002$) are almost identical with the manually calculated M^2 values following the fitted free parameter z_R of the Fixed M^2 -model ($M_{\text{x-scan}}^2 = 1.105 \pm 0.024$ and $M_{\text{y-scan}}^2 = 1.036 \pm 0.006$). This suggests as expected that both models are viable and consistent physically.

It can also be seen that the beam is slightly elliptical, since the beam waists along the x-scan $((5.72 \pm 0.05) \, \mu m)$ and y-scan $((5.50 \pm 0.01) \, \mu m)$ are not identical. This is most likely due to the aforementioned astigmatism in the beam, which is most likely caused by an improper alignment or manufacturer limitation in the triplet collimator or prime lens.

Comparing the here measured result of x-scan ($(5.72 \pm 0.05) \, \mu m$) and y-scan ($(5.50 \pm 0.01) \, \mu m$) with the theoretically calculated values from Chapter 2.1.3 Eq. 2.9 (6.166 μm), the y-scan result is less then the ideal minimal value. This suggests that the uncertainties, encountered in the calculation of the theoretical beam waist, lead to a non-ideal theoretical prediction.

Nevertheless, the experiment does satisfy the requirement of achieving a small enough beam waist.

3.2 Effects of the glass plates

As mentioned before in the main experiment the laser beams will have to travel through a window of the science chamber, which keeps the Yb-ensemble in a vacuum. In order to test and closely characterize what effects the glass windows might cause to the laser beams, the windows of the science chamber are represented by using a glass plate on a custom built glass-plate holder construction (see Fig. 2.11).

The used glass plates have a thickness of 9.525 mm according to the manufacturer and assumed refractive index n of ≈ 1.47 . The used glass plate for the test setup has no special anti-reflective coating³.

When a Gaussian beam travels through a dielectric medium, which is itself in another medium with a refractive index of 1. For example, a glass plate in air, one expects a focal waist-shift [19]. This means that the position of the beam waist will be shifted by a factor of

$$\Delta z = (1 - \frac{1}{n}) \cdot d \tag{3.8}$$

where n is the refractive index of the dielectric medium and d its thickness. This waist-shift acts in the direction of the beam propagation. Using the above parameters one can calculate the estimated theoretical waist shift

$$\Delta z = 3.045 \,\mathrm{mm} \tag{3.9}$$

It was also concluded that the glass plate should not cause a change in the beam waist size itself [19]. This means any changes that are observed, are most likely caused by textural differences on the glass plates or lenses.

Similar to the previous chapter, the normalization of Fig. 3.9 allows for a visual comparison of any asymmetries. Here the left side, clearly has a stronger relative intensity which might suggest that the beam is not perfectly aligned.

Applying the exact same method as in Chapter 3.1 and using the setup outlined in Fig. 2.7, the beam width against z-position plot in Fig. 3.10 was produced.

Checking the fit parameters in tab. 3.2 regarding the fitted Rayleigh lengths and the following beam quality factor M^2 one finds the following values;

$$z_{R,\text{x-scan}} = (0.246 \pm 0.003) \,\text{mm} \implies M^2 = \frac{\pi \left((5.85 \pm 0.05) \,\mu\text{m} \right)^2}{(0.240 \pm 0.003) \,\text{mm} \cdot 399 \,\text{nm}} \approx 1.095 \pm 0.024$$
 (3.10)

$$z_{R,y\text{-scan}} = (0.224 \pm 0.001) \text{ mm} \implies M^2 = \frac{\pi ((5.49 \pm 0.01) \, \mu\text{m})^2}{(0.232 \pm 0.001) \, \text{mm} \cdot 399 \, \text{nm}} \approx 1.022 \pm 0.006$$
 (3.11)

² This value was calculated using the Sellmeier Coefficients given by the manufacturer,https://www.corning.com/media/worldwide/csm/documents/HPFS_Product_Brochure_All_Grades_2015_07_21.pdf for a wavelength of 399 nm

³ The main experiment science chamber windows have a custom AR coating with a <1% reflection for the probe beams 399 nm

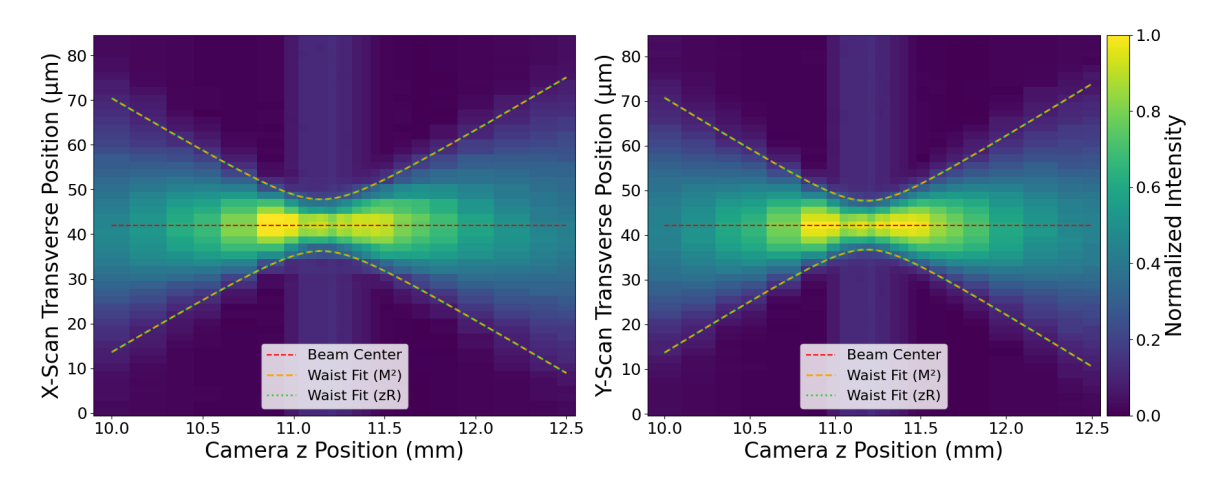


Figure 3.9: Beam width evolution along z-axis, no glass plate in beam path. Showing the transverse position, of the beam profile at different z-positions with a integral-normalized intensity color scale. Fits from Fig. 3.10 are inserted.

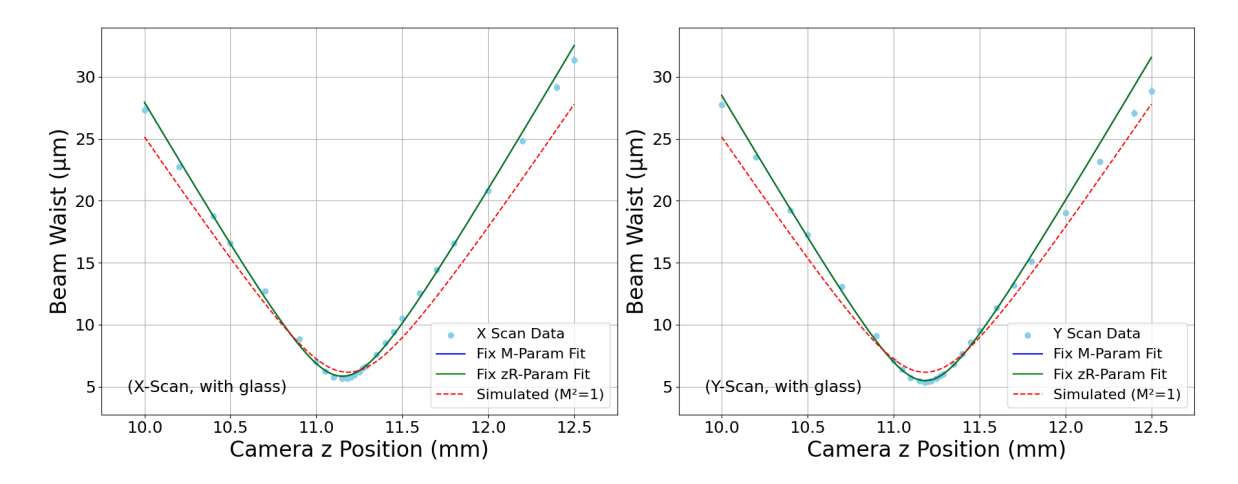


Figure 3.10: Beam width against z-position fit. The beam is propagating through a glass plate. Fit-Parameters are listed in Tab. 3.2, fitting models used are Eq. 3.2 and Eq. 3.4. The red line is the simulated fit, which is the same for all figures in this chapter. Beam width data extracted with the method method described in Chapter 3.1. The x-axis shows the z-position of the camera, which is arbitrary, but the difference in z-positions is what matters.

Axis	Fit Type	<i>w</i> ₀ [μm]	z_R [mm]	<i>z</i> ₀ [mm]	M^2
X	Fixed z_R -Param Fit Fixed M^2 -Param Fit Simulated (M^2 =1)	5.85 ± 0.05 5.85 ± 0.05 5.577	-0.246 ± 0.003 0.245	11.151 ± 0.003 11.151 ± 0.003 11.185	1.092 ± 0.006 - 1.000
Y	Fixed z_R -Param Fit Fixed M^2 -Param Fit Simulated (M^2 =1)	5.49 ± 0.01 5.49 ± 0.01 5.577	$ \begin{array}{c} - \\ 0.232 \pm 0.001 \\ 0.245 \end{array} $	11.184 ± 0.001 11.184 ± 0.001 11.185	1.021 ± 0.002 - 1.000

Table 3.2: Beam waist fit results for X and Y scans and simulation (with glass).

which are nearly identical to the values above, following the same trend as in the previous chapter, where the beam quality factors between both models are nearly identical. From the fitting parameters in Tab. 3.2 a few conclusions can be made, firstly investigating the waist shift between $z_{0,\text{no glass}} - z_{0,\text{with glass}} = \Delta z$ one finds;

$$z_{0,\text{no glass}} - z_{0,\text{with glass}} = (3.086 \pm 0.004) \,\text{mm}$$
 (3.12)

Y-Scan:

$$z_{0,\text{no glass}} - z_{0,\text{with glass}} = (3.072 \pm 0.001) \,\text{mm}$$
 (3.13)

So comparing the results from Eq. 3.9 and Eq. 3.12/3.13, the values would suggest that the glass plate either has a slightly lower refractive index or slightly bigger thickness, less then 5% change on either one. This is within the expected range of error, considering the parameters of the test experiment and the manual set up and alignment.

Next, when comparing the beam waists (see Tab. 3.1 and Tab. 3.2) between the measurement with and without the glass, a slight decrease of $0.01\,\mu m$ (y-scan) to $0.13\,\mu m$ (x-scan) could be observed, however as mentioned before, this is not an effect explicitly due to the glass plate, but rather due to introduced aberrations. Same goes for the beam quality, only negligible changes could be observed, which are not of direct physical consequence caused by the glass.

This concludes, that the only significant change that is caused by the glass plates is the waist-shift according to Eq. 3.8. Nothing besides this would then be expected to happen in the actual main experiment, while the beam waist is still satisfyingly small.

3.3 Re-collection of probe light

After focusing, the beam passes through a beam path with the same optical components as the input arm, arranged in reverse sequence, before being coupled into a re-collection fiber, as seen in Fig. 2.7. This is important considering the goal of the main experiment. Since the goal is to measure and analyze photons that have interacted with the Yb-ensemble, it is important that the setup allows for a high re-collection coupling efficiency. Additionally, this re-coupling allows for the quantification of possible aberrations, a high single-mode fiber to single-mode fiber coupling efficiency implies a high beam quality.

The same alignment and coupling procedure described in Chapter 2.2.2 is followed. To characterize the losses introduced by individual optical elements, power measurements are performed using the same calibrated power meter throughout the experiment to ensure consistency.

Explicitly providing uncertainties for the measured powers proves itself to be quite challenging. Since there are a large number of varying variables like the surface quality of optical components, dust contamination, laser beam stability, power meter sensitivity and fiber alignment accuracy, accurately quantifying each contribution to the uncertainty cannot be reliably done. Therefore such statements about the uncertainties of the measured powers could not be done to any meaningful capacity.

The coupling efficiency (abbreviated as "CE" in the following) is determined as the ratio of the power at the input of the fiber coupler to the power successfully coupled into the fiber. This should not be confused with the ratio of the total input power into the system, with the coupled power into the second fiber.

To couple into the same optical fiber as in the beginning [9], a triplet collimator [11] of the same model is used as described in Chapter 2.1.3. However, when starting these measurements of the CE, it was observed that the free space coupling was much lower than expected (only about $\approx 60\%$). But with the triplet collimator came an efficiency card provided by the manufacturer stating that the collimator should provide a CE of up to $\approx 80\%$.

This discrepancy most likely comes from the fact that the beam coming out of the collimator, was not as well collimated, likely stemming from an improper fiber-lens distance of the coupling triplet collimator.

Because of this the fiber-lens distance inside the collimator was manually moved and adjusted and thus became another degree of freedom to the coupling algorithm, see Chapter 2.2.2. Adjusting the fiber adapter position was reasonable because the beam exiting the first fiber coupler was likely less collimated than the beam achieved using the two-lens configuration.

3.3.1 Triplet Collimator Adjustment

The triplet collimator is constructed by a larger lens casing and a smaller fiber adapter casing, see Fig. 3.11. The fiber adapter is placed inside the larger casing and then glued. Therefore in order to change the distance between the fiber adapter and the lenses inside, this glue needs to be removed and the adapter distance manually adjusted.

For this several methods are used;

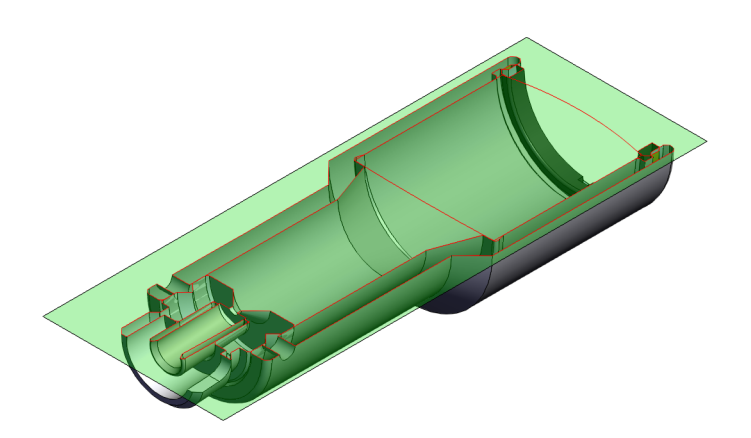
• Placing the triplet collimator in an ultrasonic acetone bath for 30 min, making sure that no lenses would come into contact with the acetone.

- Using a heat gun on the glued area.
- Periodically using a pointy tool, like surgical tweezers to remove layers of the glue, while applying drops of acetone on the glued areas.
- Using a flathead screwdriver to push the adapter piece out by hand. In order not to damage the threading of the adapter, a nut is screwed on which helps in pushing the adapter piece off. This was the method that seemed to lead to a success the fastest.

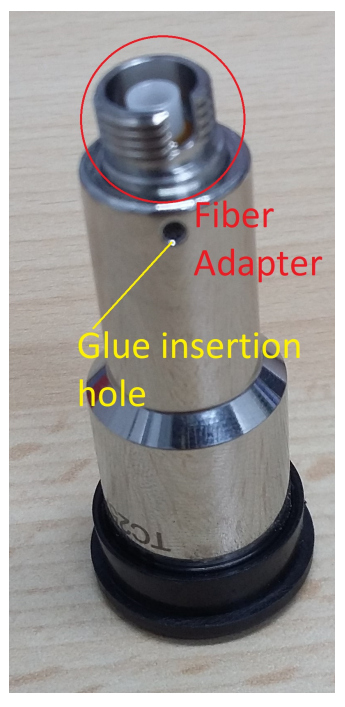
With the glue removed successfully, the position of the fiber adapter can now be manually adjusted. However the unglued fiber adapter was quite loose (see images of separated parts in Fig. 3.11(c)) and as such the exact fiber adapter position was highly sensitive and difficult to reproduce reliably. Nonetheless, the possibility to adjust the fiber adapter position lead to an improved CE. For freespace-coupling a CE of 78.4% was reached, which is close to the roughly 80% specified by the manufacturer. When the lenses and the glass plates were positioned along the beam path, a CE of 82.4% was reached—actually higher than freespace CE—suggesting that the lenses lead to a better collimation than the triplet collimators. The collimation was checked with a shear plate interferometer, but the difference was too small to be identified with it.

Additionally the transmission of the two used lenses was measured, for the first lens a transmission of 97.6% was measured and for the second lens 95.9%. This slight difference will be due to environmental factors like dust or imperfections on the lens surfaces, thus suggesting a loss of beam power of around 6.5% due to the lenses alone. The transmission of the glass plates was also investigated, it was found that it is approximately 87.3%. This means total transmission of about $T_{\text{total}} = T_{\text{lens1}} \cdot T_{\text{lens2}} \cdot T_{\text{glass-plates}} = 81.7\% \implies \text{leading to a loss of } 18.3\% \text{ due to all the optical elements used.}$

Finally, it can be concluded that by adjusting the fiber adapter position inside the triplet collimator a CE of 82.4% was reached and that the transmission through the glass plates and lenses is 81.7%.



(a) Triplet collimator with fiber adapter piece. Section cut to view internal structure. Image adapted from the technical drawing provided by the manufacturer at https://www.thorlabs.com/thorproduct.cfm?partnumber=TC25APC-405. Edited image taken from YQO-Lab



(b) Triplet collimator with fiber adapter and lenses, used to re-collect the probe light into a single-mode fiber. Before disassembly, the glue insertion hole is marked.



(c) Triplet collimator with separated fiber adapter; one of the three lenses in the lens system is marked.

Figure 3.11: Views of the TC25APC-405 triplet collimator, including internal CAD rendering (top) and photographic documentation before and after separation (bottom).

Conclusion

In this thesis the goal was to test how to produce a better beam geometry which could then be reproduced in the Yb-NQO few-photon main experiment. For this a test setup of the main experiment was built with which the relevant optical elements were as closely reproduced as possible. Improving the beam geometry will lead to a reduction in the dimensionality of the excitation volume from three dimensions to just one. So the reducing of the beam waist size helps will the goal of creating an only one-dimensional Rydberg-atom chain.

Firstly, it was outlined how the test setup was constructed (see Fig. 2.2 and 2.7) and how the alignment of each component was performed, outlined in Chapter 2.2.2/3.1. The choice of the most critical optical components was motivated by the need to achieve a small beam waist, and the arguments were outlined in Chapter 2.1.3.

During experimentation it was found that the camera used to analyze the beam, needed a calibration method to account for a Bayer Pattern[14]. The code to utilize the camera for analysis had already been written by Samuel Germer in his Bachelor Thesis[13], the method that was used to process the images and adjust them for the probe beam wavelength of 399 nm was outlined in Chapter 3.1. The used method allows for a strong reduction in said pattern, leading to a higher analysis quality.

The final achieved beam waist was measured to be around $w_0 = (5.72 \pm 0.05) \, \mu m$ in the x-scan and $w_0 = (5.50 \pm 0.01) \, \mu m$ in the y-scan, as shown in Fig. 3.8 and Tab. 3.1. The impact of the glass plate on the beam was investigated in Section 3.2, and it was found that the beam waist was slightly increased to $w_0 = (5.85 \pm 0.05) \, \mu m$ in the x-scan and $w_0 = (5.49 \pm 0.01) \, \mu m$ in the y-scan, as shown in Fig. 3.10 and Tab. 3.2, however it was concluded according to [19] that this increase is not caused by the glass plate itself, but rather by irregularities on the optical surfaces.

These achieved beam waists fulfil the desires of the main experiment of around being $\lesssim 6 \,\mu\text{m}$ (see Chapter 2.1.1) from the provided theoretical ideal in Eq. 2.9.

The beam quality factors were determined to be around $M^2 \approx 1.104 \pm 0.006$ in the x-direction and $M^2 = 1.035 \pm 0.002$ in the y-direction, without the glass plate, and around $M^2 = 1.092 \pm 0.01$ in the x-scan and $M^2 = 1.021 \pm 0.01$ in the y-scan with the glass plate, showing that the beam quality did not change significantly due to the glass plate.

The glass plate's main effect on the beam was a shift along the z-axis of the waist position[19], which was found to be around $\Delta z = (3.086 \pm 0.004)$ mm (Eq. 3.12) in the x-scan and $\Delta z = (3.072 \pm 0.001)$ mm (Eq. 3.13) in the y-scan, in accordance with the theoretical prediction of [19] in Eq. 3.9.

Finally, the coupling efficiency into a single-mode fiber[9] was measured to be around CE = 82.4% using the triplet collimator [11], while the losses introduced by the optical elements were estimated to be around $Loss_{total} = 18.3\%$. Concluding from which exact factors these high losses come from, be it from misalignment, a lack of anti-reflective coating (Fresnel losses) or other aberrations, was not made.

Even though the theoretical prediction for the ideally minimal beam waist contains some inaccuracies, the beam waists of the y-scans with and without the introduction of a glass plate in the beam path, is satisfyingly small- showing that a small enough beam waist can be produced, which can then be implemented in the main experiment.

Outlook

The next steps in the main experiment involve ensuring that the new beam waist of the probe beam is small enough to lie entirely within the spatial extent of the control beam waist (see Fig. 2.7 for the setup sketch). This ensures uniform control-field coupling across the entire probe volume and prevents spatially varying optical effects.

The main benefit demonstrated here is that the probe beam waist can be reduced without requiring new optical components or significant modifications to the existing experimental infrastructure. This means that the alignment strategies and waist-reduction methods applied here can be directly implemented in the main Rydberg experiment.

As a result, it becomes possible to reliably excite lower principal quantum number states (see Fig. 2.5 for the Rydberg blockade radius as a function of n). For the old beam waist a n-state of $n \approx 155$ would be needed, while for the new beam waist of 5.5 µm only a n-state of around $n \approx 120$ is necessary (shown in Fig. 2.5 figure shows a new beam waist of 5.6 µm, that result would not deviate greatly from the 5.5 µm however). Only approximate n-states are mentioned, since the exact n-state would change dramatically with the choice of the of the Rabi-frequency for example.

This is beneficial because the Rydberg blockade radius scales as $r_B \propto \sqrt[6]{C_6}$, and the van der Waals coefficient $C_6 \propto n^{11}$. Additionally, the electric polarizability of a Rydberg ensemble scales as $\mu \propto n^7$.

Reducing n therefore decreases the ensemble's sensitivity to stray electric fields, thereby improving experimental control and reproducibility. Moreover, since the new probe beam waist satisfies the condition $r_B \ge 2 \cdot w_0$, all Rydberg atoms within the probe volume will block the excitation of nearby atoms to the same Rydberg state. This effectively constrains the system to a one-dimensional geometry in the axial direction, significantly reducing the experimental complexity.

APPENDIX A

Appendix

A.1 Gaussian fits for beam profile measurements

The Gaussian fits belonging to the beam width z-axis progression in Fig. 3.6. can be seen in Fig. A.1 and A.2.

A.2 Beam profile

From the beam profiles that were taken(see Fig. A.3), the minor axis will be generally considered to be the beam diameter, though the minor and major axis are roughly the same.

A.3 Beam quality factor M^2

Here a few figures are shown to give an intuition on how the beam quality factor M^2 impacts the beam waist and divergence angle. According to Eq. 3.2 using the following parameters, $w_0 = 5.5 \,\mu\text{m}$, $\lambda = 399 \,\text{nm}$ the plots in Fig. A.4 are produced.

Additionally the divergence angle can be plotted using Eq. 3.3 and the following parameters, $w_0 = 5.5 \,\mu\text{m}$, $\lambda = 399 \,\text{nm}$. The results can be seen in Fig. A.5.

A.4 Triplet Collimator Focal Length Calculation

In order to extract the focal length for the TC25-APC-405 triplet collimator, the focal lengths and alignment wavelengths for other collimators was extrapolated to estimate the focal length for the used collimator at a wavelength of 399 nm. This was done by using a Taylor-Expansion model to the third order around 405 nm, outlined in Eq. A.1

$$\Delta \lambda = a + b(\lambda - 405) + c(\lambda - 405)^{2} + d(\lambda - 405)^{3}$$
(A.1)

This model was able to accurately reproduce the values specified by Thorlabs from which it was concluded that the estimation for the desired wavelength is valid. Tab. A.1 shows some example

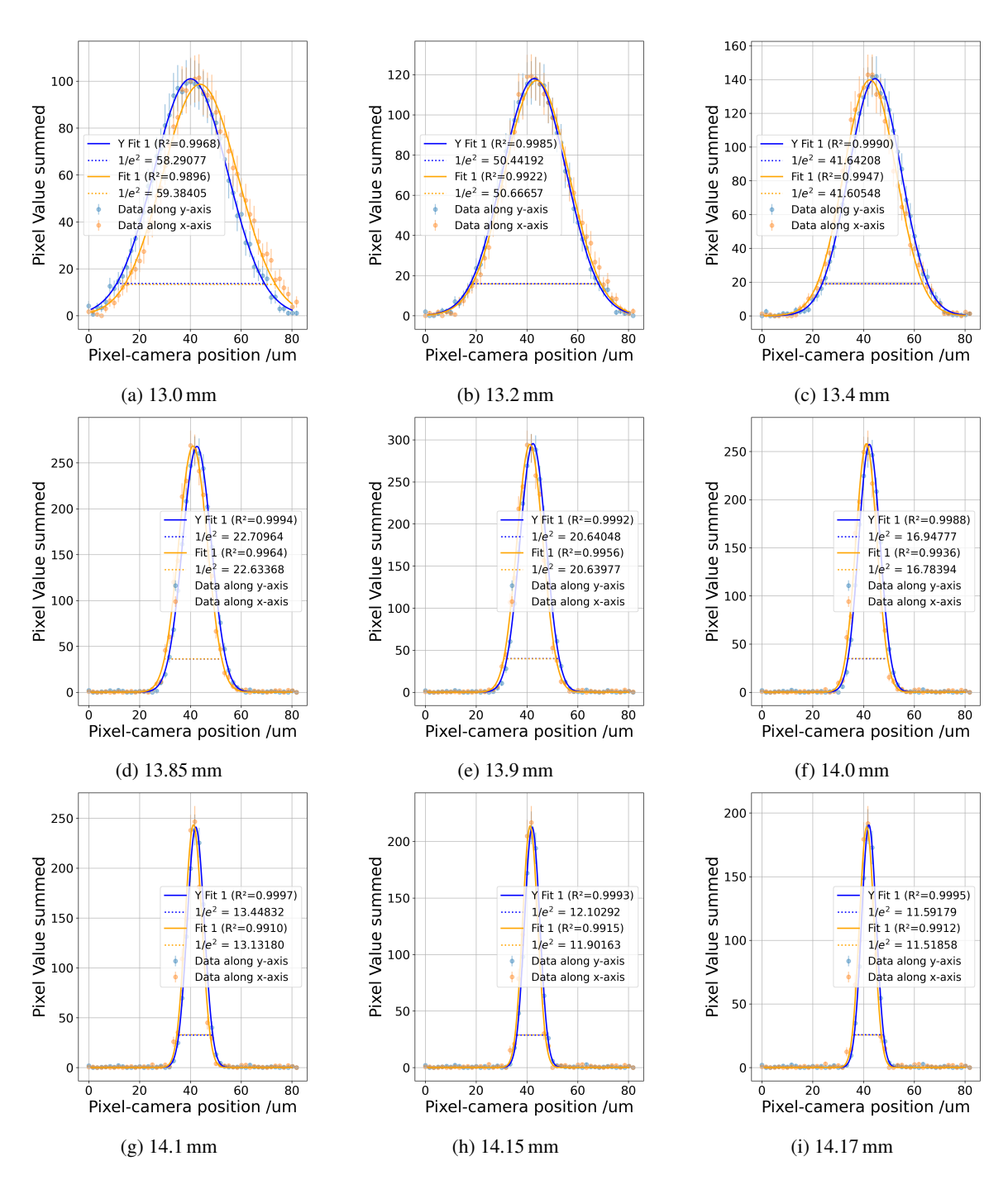


Figure A.1: Gaussian fits at increasing *z*-positions from 13.0 mm to 14.17 mm (no glass).

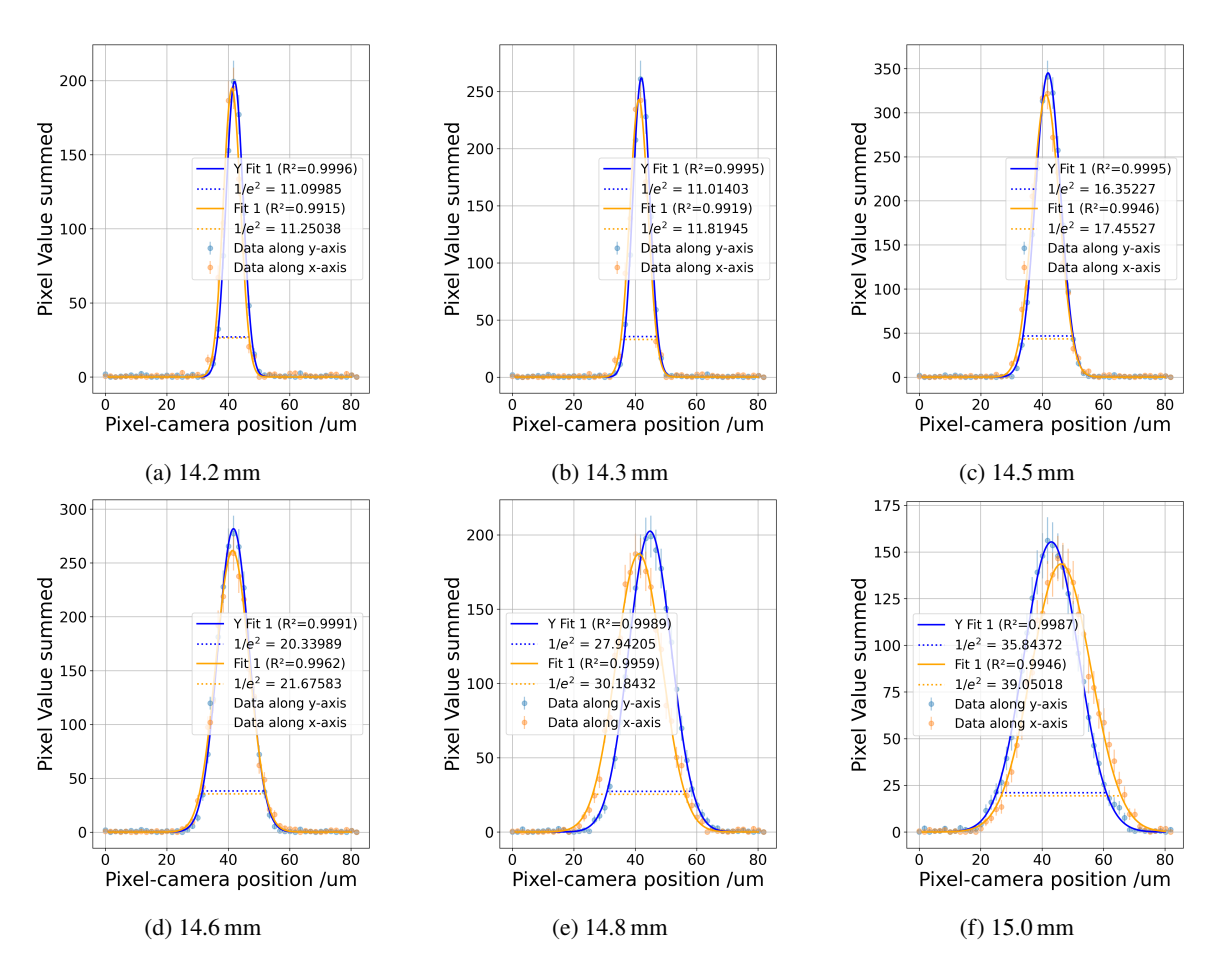
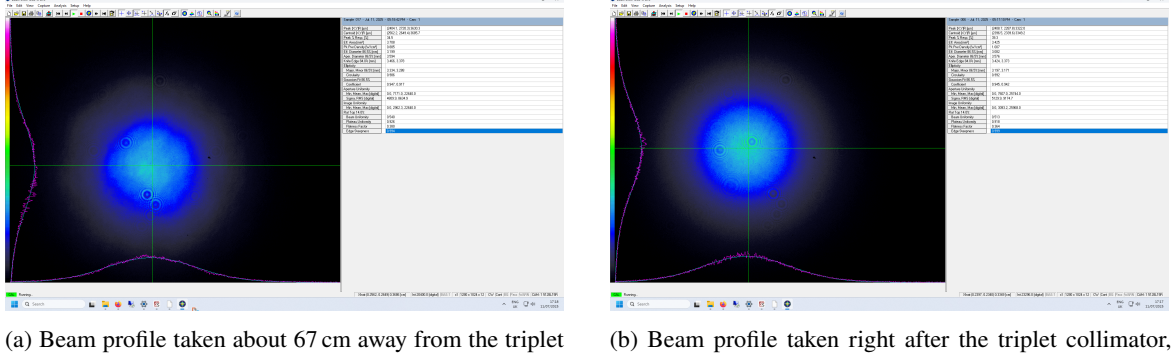


Figure A.2: Continuation of Gaussian fits from 14.2 mm to 15.0 mm (no glass). These are part of the beam waist progression shown in Fig. 3.6.



collimator, major axis 3.334 mm, minor axis 3.288 mm, effective diameter(86.5% intensity) of 3.199 mm

(b) Beam profile taken right after the triplet collimator, major axis 3.197 mm, minor axis 3.171 mm, effective diameter(86.5% intensity) of 3.082 mm

Figure A.3: Comparison of beam profiles at different positions

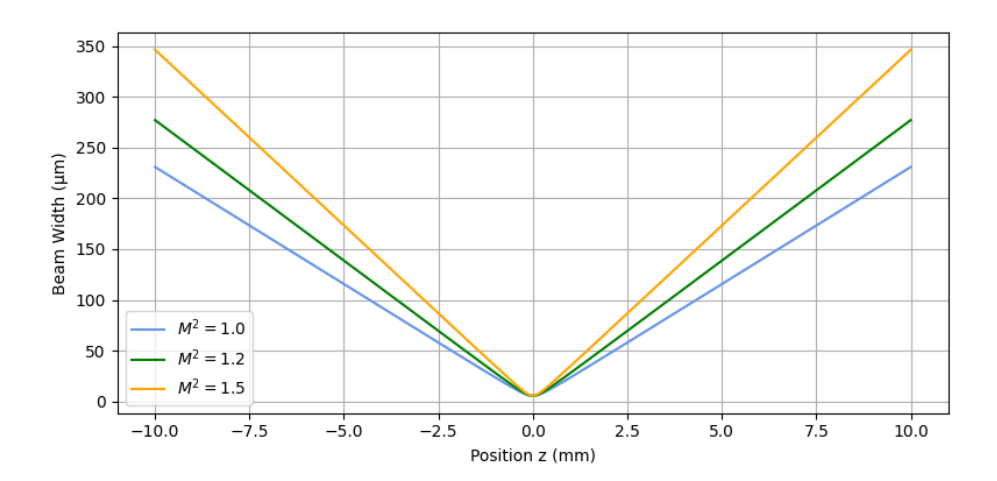


Figure A.4: Different beam widths against z-axis position, for different M^2 values, with $w_0 = 5.5 \,\mu\text{m}$, $\lambda = 399 \,\text{nm}$, plots made according to Eq. 3.2.

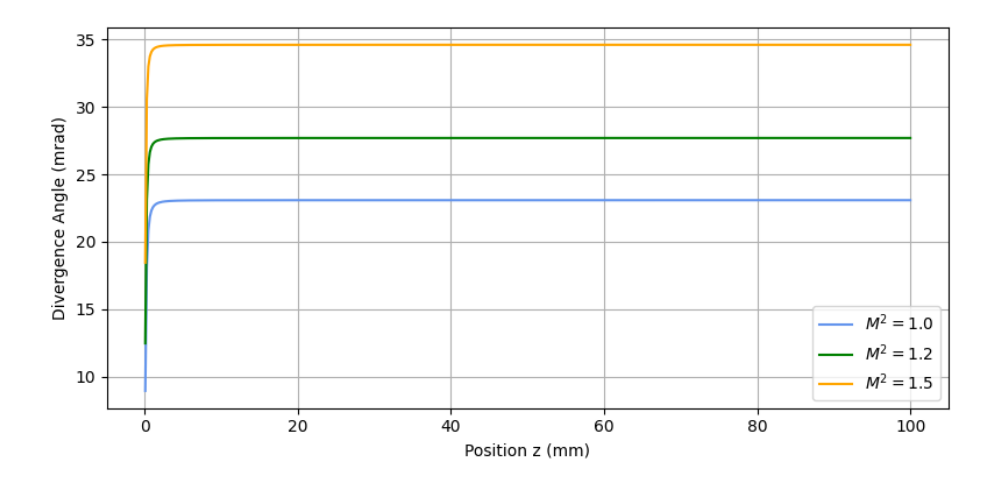


Figure A.5: Different beam divergence angles against z-axis position, for different M^2 values, with $w_0 = 5.5 \,\mu\text{m}$, $\lambda = 399 \,\text{nm}$, plots made according to Eq. 3.3.

values are listed, that were produced by using the above model and the ones specified by Thorlabs. A figure of the data points and the used fit is also shown in Fig. A.6

Table A.1: Focal Lengths from Taylor Fit vs. Thorlabs Specifications

Wavelength (nm)	Taylor Fit Focal Length (mm)	Thorlabs Specified Focal Length (mm)
399	24.765	_
405	24.772	24.77
543	24.910	24.91
633	24.987	24.98

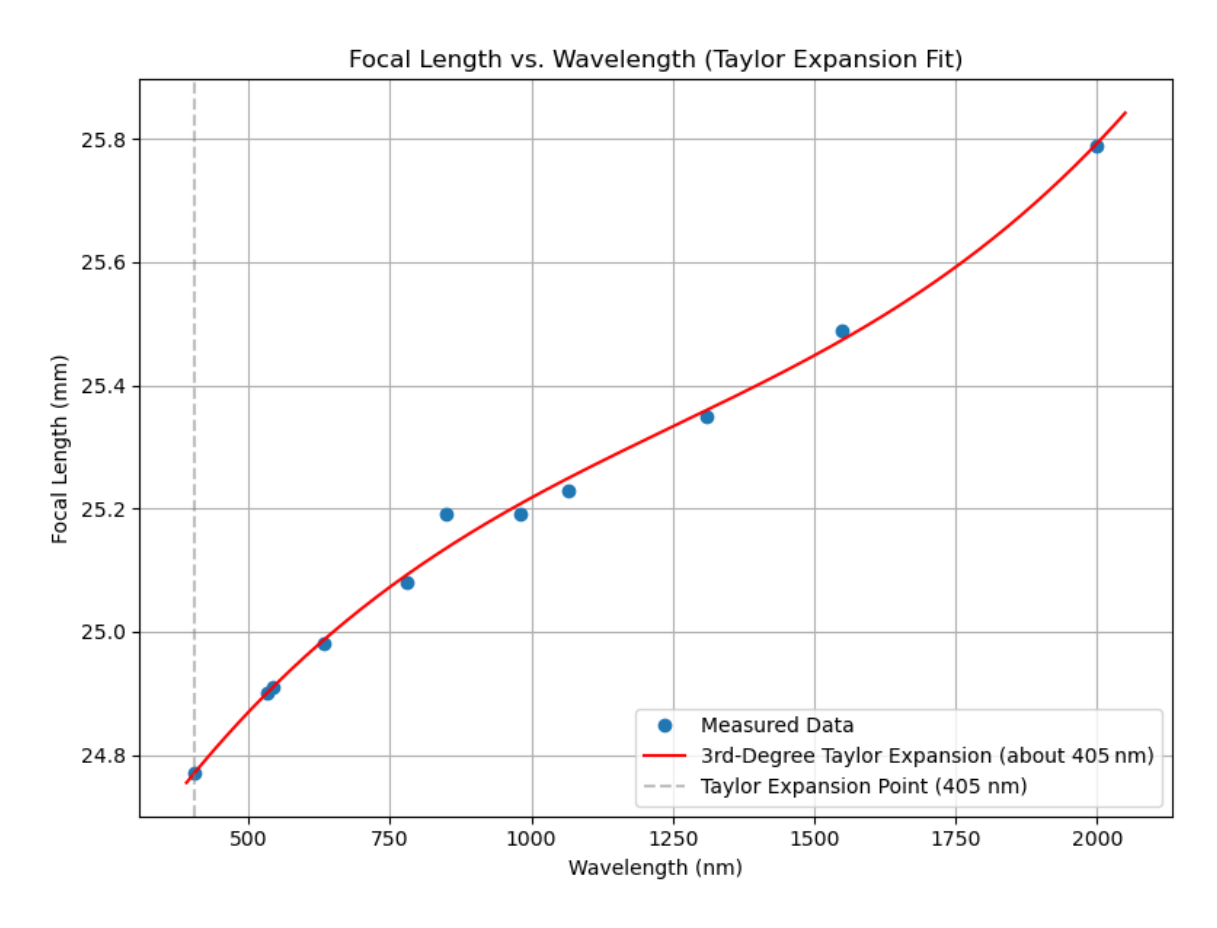


Figure A.6: Data points extracted from https://www.thorlabs.com/newgrouppage9.cfm?objectgroup_id=5124&pn=TC25FC-405. Shown is a fit by using a Taylor Expansion model(see Eq. A.1) to predict a desired—but not specified focal length—at 399 nm.

Bibliography

```
[1] P. R. Berman, H. Nguyen and A. G. Rojo,
Theory of the Rydberg blockade with multiple intermediate-state excitations,
Phys. Rev. A 105 (4 2022) 043715,
URL: https://link.aps.org/doi/10.1103/PhysRevA.105.043715 (cit. on pp. 1, 3).
```

- [2] G. Higgins, "Two-Photon Rydberg Excitation", *A Single Trapped Rydberg Ion*, Cham: Springer International Publishing, 2019 43, ISBN: 978-3-030-33770-4, URL: https://doi.org/10.1007/978-3-030-33770-4_4 (cit. on p. 1).
- [3] Edmund-Optics, Edmund Optics online shop,
 URL: https://www.edmundoptics.eu/p/125mm-dia-x-75mm-fl-vis-nir-coated-achromatic-lens/9705/ (visited on 10/07/2025) (cit. on pp. 3, 9, 11).
- [4] J. Kumlin et al., *Quantum optics with Rydberg superatoms*, Journal of Physics Communications 7 (2023) 052001, URL: https://dx.doi.org/10.1088/2399-6528/acd51d (cit. on p. 3).
- [5] D. Meschede, "Optik, Licht und Laser", 3rd ed., Wiesbaden, Germany: Vieweg & Teubner Verlag, 2008, chap. 2.3 48, ISBN: 978-3-8348-9288-1, URL: https://link.springer.com/book/10.1007/978-3-8348-9288-1 (cit. on pp. 5, 6, 9).
- [6] Edmund-Optics, Gaussian Beam Propagation, https://www.edmundoptics.com/knowledge-center/application-notes/lasers/gaussian-beam-propagation/, Accessed: 2025-07-11, 2023 (cit. on p. 7).
- [7] S. A. Self, Focusing of Spherical Gaussian Beams, Applied Optics 22 (1983) 658 (cit. on p. 6).
- [8] S. Ma et al., Universal Gate Operations on Nuclear Spin Qubits in an Optical Tweezer Array of ¹⁷¹Yb Atoms, Physical Review X 12 (2022), ISSN: 2160-3308, URL: http://dx.doi.org/10.1103/PhysRevX.12.021028 (cit. on p. 8).
- [9] OZ Optics, QPMJ/PMJ Fiber-Optic Polarization-Maintaining Patch-Cable Datasheet, Accessed July 18, 2025, OZ Optics, 2024, URL: https://shop.amstechnologies.com/media/89/e1/ac/1720718100/PMJ-QPMJ-PM-Patch-Cables-OZ-Optics-Datasheet.pdf (cit. on pp. 9, 32, 36).

- [10] R. Paschotta, *Fiber Collimators*, https://www.rp-photonics.com/fiber_collimators.html, Accessed: 2025-07-11. Encyclopedia entry at RP Photonics AG, 2013 (cit. on p. 9).
- [11] Thorlabs, Inc., TC25APC-405 405 nm Triplet Fiber-Optic Collimator Datasheet, Accessed July 18, 2025, Thorlabs, Inc., 2025, URL: https://www.thorlabs.com/thorproduct.cfm?partnumber=TC25APC-405 (cit. on pp. 11, 32, 36).
- [12] K. S. Mobarhan, M. Hagenbuechle and R. Heyler, *Fiber to Waveguide Alignment Algorithm*, Application Note DS-03002-App-Note-6, Accessed: 2025-07-14: Newport Corporation, 2025, URL: https://www.newport.com/medias/sys_master/images/images/h57/hc5/9135932669982/DS-03002-App-Note-6.pdf (cit. on pp. 16, 17).
- [13] S. Germer, Frequency stabilization of a laser and a high resolution optical setup for excitation of ultracold Rydberg atoms, Bachelorarbeit in Physik: Institut für Angewandte Physik, Universität Bonn, 2023 (cit. on pp. 19, 35).
- [14] Silicon Imaging, Inc., *RGB "Bayer" Color and MicroLenses*, Accessed July 15, 2025, n.d. URL: https://www.siliconimaging.com/RGB%20Bayer.htm (cit. on pp. 19, 35).
- [15] B. E. Bayer, "Color imaging array", Patent U.S. Patent 3,971,065, Filed Jun 10, 1974; issued Jul 20, 1976, 1976, URL: https://patentimages.storage.googleapis.com/89/c6/87/c4fb7fbb6d0a0d/US3971065.pdf (cit. on p. 19).
- [16] A. Gnanasambandam and S. H. Chan,

 Exposure-Referred Signal-to-Noise Ratio for Digital Image Sensors,

 arXiv preprint arXiv:2112.05817 (2021), Appendix VIII-A confirms photon arrival follows a

 Poisson distribution and its Gaussian approximation for high flux,

 URL: https://arxiv.org/abs/2112.05817 (cit. on p. 19).
- [17] Zemax LLC, How to convert FWHM measurements to 1/e² halfwidths, Accessed: 2025-07-24, 2021, URL: https://support.zemax.com/hc/en-us/articles/1500005488161-How-to-convert-FWHM-measurements-to-1-e-2-halfwidths (cit. on p. 23).
- [18] A. E. Siegman, *How to (Maybe) Measure Laser Beam Quality*, Edward L. Ginzton Laboratory, Stanford University, 1997 (cit. on p. 26).
- [19] S. Nemoto, Waist shift of a Gaussian beam by a dielectric plate, Appl. Opt. 28 (1989) 1643 (cit. on pp. 29, 35).

List of Figures

2.1	Level scheme of the Yb-Rydberg atoms used in the experiment. The probe beam drives from the $6s6s^1S_0$ ground state to the excited state, the control beam will drive from the excited state to the $6sns1_0^S$ Rydberg state, in the YQO experiment a 395 nm	
2.2	laser is used. Image taken from YQO-Lab. Main experiment setup sketch of the optical beam paths of the probe(blue) and control(purple) lasers. Both beams are lead through the science chamber and then	4
2.3	recollected on a mirrored side. Image taken from YQO-Lab	6
2.4	Gaussian beam and intensity profile and the corresponding gaussian fit, figure taken from [6].	7
2.5	Rydberg-blockade radius against principle quantum number n, for $\Omega_{\rm eff} = 5$ Mhz. Calculation provided by the YQO-Lab. With $w_{0,\rm old} = 8.3~\mu \rm m$ and $w_{0,\rm new} = 5.6~\mu \rm m$. Image taken from YQO-Lab	8
2.6	Screenshot of a simulation program which calculates a 399 nm laser beam propagating through two lenses. The first lens has a focal length of 24.76 mm (triplet collimator, left) and the second lens a focal length of 74.82 mm (prime lens adjusted for wavelength focal shift, right). The simulation assumes a MFD of 4.08 μ m (left minimal point) and predicts a final beam waist of $\approx 6.179 \mu$ m (right minimal point). The text box at	1.0
2.7	the bottom right, is simply used to scale the simulation picture for better visualization. Test setup sketch to simulate main experiment. The beam is lead through ND filters to reduce the intensity of the beam onto the camera and prevent any damage, but also not reduced too low, to lose a good signal to noise ratio. Afterwards, the beam is coupled into a fiber, collimated with a triplet collimator[11] and then focused by an achromatic lens[3] with a focal length of 75 mm. After passing the glass plates, the focused beam is re-collimated by a second lens of the same kind and then coupled back into a second fiber. Both fiber couplers are mounted on optical mounts and have	
2.8	the same triplet collimator[11]	11 12
2.9	Custom designed lens mount, with lens holder on a z-axis translation stage with micrometer precision adjustment screw tool. Image taken from YQO-Lab	13

2.10	Picture taken of the camera on a z-axis translation stage, which allows for micro-meter adjustments in identifying the beam waist position. With the glass plate and ND filter visible too	14
2.11	Custom built mirror-holders to hold the glass plate in place. Two mechanical pieces, hold the glass plates with rubber tips to avoid any damages. Beam propagates roughly through the vertical center of the glass plates	15
2.12	Symbolic image of "hill climbing" algorithm and a local and absolute peak. Image taken form [12]	17
3.1	Uncalibrated (right) and calibrated (left) image taken with the same camera as outlined above. Checkerboard Bayer-pattern can be seen in the uncalibrated image	20
3.2	Camera image calibration method flowchart	21
3.3	Linear fits used for extracting the scaling factors, for the y-scan (left) and x-scan (right). Data points are the mean values of the x,- and y-scanned sums of the homogeneously illuminating beam against different exposure times, covering the range of the camera. Errors are calculated by taking the Poisson-error distribution into account, so taking $\Delta N = \sqrt{N}/\sqrt{\text{number of pixels}}$. Since both scans are almost identical, there seems to be no systematic error in the pixel gain settings.	22
3.4	Beam waist extraction method flowchart	24
3.5	Beam image and corresponding Gaussian fit 3.1 at 13.85 mm (no glass). The Gaussian fit in Fig. 3.5(b) shows a dotted line, which is at the position of the $1/e^2$ width, for both fits the quality factor R^2 shows how well the fit fits to the data, ideally $R^2 = 1$. This z-position was chosen to for no particular reason other then being clearly visible.	24
3.6	Beam profile evolution along propagation axis at increasing z-positions from 13.0 mm (first image of measurement) to 15.0 mm(last image of measurement), no glass in the beam path. Each image uses a relative color scale, which shows the camera pixel value, after calibration. Each pixel has a size of $1.67 \mu m \times 1.67 \mu m$. The axis show the pixel position of the beam on the camera, the image is automatically centered to	25
2.7	the brightest point of the beam.	25
3.7	Beam width evolution along z-axis, no glass plate in beam path. Showing the transverse position, of the beam profile at different z-positions with a integral-normalized intensity color scale. Fits from Fig. 3.8 are inserted.	26
3.8	Beam width against z-position fits. The beam is not propagating through a glass plate. Fit-parameters are listed in tab. 3.1, fitting models used are Eq. 3.2 and Eq. 3.4. The red line is the simulated fit, which is the same for all figures in this chapter. The beam width data is extracted from the beam profile images in Fig. 3.6. The x-axis shows the z-position of the camera, which is arbitrary, but the difference in z-positions is what matters.	27
3.9	Beam width evolution along z-axis, no glass plate in beam path. Showing the transverse position, of the beam profile at different z-positions with a integral-normalized intensity	_,
	color scale. Fits from Fig. 3.10 are inserted	30

3.10	Beam width against z-position fit. The beam is propagating through a glass plate.	
	Fit-Parameters are listed in Tab. 3.2, fitting models used are Eq. 3.2 and Eq. 3.4. The	
	red line is the simulated fit, which is the same for all figures in this chapter. Beam	
	width data extracted with the method method described in Chapter 3.1. The x-axis	
	shows the z-position of the camera, which is arbitrary, but the difference in z-positions	
	is what matters	30
3.11	Views of the TC25APC-405 triplet collimator, including internal CAD rendering (top)	
	and photographic documentation before and after separation (bottom)	34
A .1	Gaussian fits at increasing z-positions from 13.0 mm to 14.17 mm (no glass)	38
A.2		50
11.2	the beam waist progression shown in Fig. 3.6	39
A.3		39
A.4	Different beam widths against z-axis position, for different M^2 values, with $w_0 =$	5)
71.7		40
A.5	2	70
Α.3	$w_0 = 5.5 \mu\text{m}, \lambda = 399 \text{nm}, \text{plots made according to Eq. 3.3.} \dots \dots$	40
۸ 6	Data points extracted from https://www.thorlabs.com/newgrouppage9.cfm?	40
A.6	*	
	objectgroup_id=5124&pn=TC25FC-405. Shown is a fit by using a Taylor Ex-	
	pansion model(see Eq. A.1) to predict a desired—but not specified focal length—at	41
	399 nm	41

List of Tables

	Beam waist fit results for X and Y scans and simulation	
A 1	Focal Lengths from Taylor Fit vs. Thorlabs Specifications	41

Used tools and resources

The following tools and resources and their use for the production of this thesis are listed here;

- ChatGPT-40 was used for the help in text production, mainly for helping with clarity, grammar and spelling.
- Python was used in a JupyterHub and local JupyterNotebook environment for the data analysis.
- Inkscape and Microsoft Paint were used for the production of some of the images.
- GaussianBeam was used for the Gaussian beam simulation.